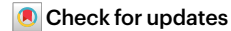
# The complex circumstellar environment of supernova 2023ixf

https://doi.org/10.1038/s41586-024-07116-6

Received: 3 October 2023

Accepted: 24 January 2024

Published online: 27 March 2024



E. A. Zimmerman<sup>1,29 \infty</sup>, I. Irani<sup>1,29</sup>, P. Chen<sup>1</sup>, A. Gal-Yam<sup>1</sup>, S. Schulze<sup>2</sup>, D. A. Perley<sup>3</sup>, J. Sollerman<sup>4</sup>, A. V. Filippenko<sup>5</sup>, T. Shenar<sup>6</sup>, O. Yaron<sup>1</sup>, S. Shahaf<sup>1</sup>, R. J. Bruch<sup>1,7</sup>, E. O. Ofek<sup>1</sup>, A. De Cia<sup>8,9</sup>, T. G. Brink<sup>5</sup>, Y. Yang<sup>5,10</sup>, S. S. Vasylyev<sup>5</sup>, S. Ben Ami<sup>1</sup>, M. Aubert<sup>11</sup>, A. Badash<sup>1</sup>, J. S. Bloom<sup>5</sup>, P. J. Brown<sup>12</sup>, K. De<sup>13</sup>, G. Dimitriadis<sup>14</sup>, C. Fransson<sup>4</sup>, C. Fremling<sup>15,16</sup>, K. Hinds<sup>3</sup>, A. Horesh<sup>17</sup>, J. P. Johansson<sup>2</sup>, M. M. Kasliwal<sup>16</sup>, S. R. Kulkarni<sup>16</sup>, D. Kushnir<sup>1</sup>, C. Martin<sup>18</sup>, M. Matuzewski<sup>18</sup>, R. C. McGurk<sup>19</sup>, A. A. Miller<sup>20,21</sup>, J. Morag<sup>1</sup>, J. D. Neil<sup>16</sup>, P. E. Nugent<sup>5,22</sup>, R. S. Post<sup>23</sup>, N. Z. Prusinski<sup>18</sup>, Y. Qin<sup>16</sup>, A. Raichoor<sup>5</sup>, R. Riddle<sup>15</sup>, M. Rowe<sup>12</sup>, B. Rusholme<sup>24</sup>, I. Sfaradi<sup>17</sup>, K. M. Sjoberg<sup>25,26</sup>, M. Soumagnac<sup>22,27</sup>, R. D. Stein<sup>16</sup>, N. L. Strotjohann<sup>1</sup>, J. H. Terwel<sup>14,26</sup>, T. Wasserman<sup>1</sup>, J. Wise<sup>3</sup>, A. Wold<sup>24</sup>, L. Yan<sup>15</sup> & K. Zhang<sup>5,28</sup>

The early evolution of a supernova (SN) can reveal information about the environment and the progenitor star. When a star explodes in vacuum, the first photons to escape from its surface appear as a brief, hours-long shock-breakout flare<sup>1,2</sup>, followed by a cooling phase of emission. However, for stars exploding within a distribution of dense, optically thick circumstellar material (CSM), the first photons escape from the material beyond the stellar edge and the duration of the initial flare can extend to several days, during which the escaping emission indicates photospheric heating<sup>3</sup>. Early serendipitous observations<sup>2,4</sup> that lacked ultraviolet (UV) data were unable to determine whether the early emission is heating or cooling and hence the nature of the early explosion event. Here we report UV spectra of the nearby SN 2023ixf in the galaxy Messier 101 (M101). Using the UV data as well as a comprehensive set of further multiwavelength observations, we temporally resolve the emergence of the explosion shock from a thick medium heated by the SN emission. We derive a reliable bolometric light curve that indicates that the shock breaks out from a dense layer with a radius substantially larger than typical supergiants.

On 19 May 2023, SN 2023ixf was discovered in the nearby (distance  $6.9 \pm 0.12 \,\mathrm{Mpc})^5$  galaxy M101 by K. Itagaki<sup>6</sup> at 17:27:15 (UTC dates are used throughout this paper), and it was reported to the Transient Name Server (https://www.wis-tns.org/object/2023ixf) at 21:42:21. The new object is located at right ascension  $\alpha = 14 \text{ h} \cdot 03 \text{ min } 38.56 \text{ s}$  and declination  $\delta = 54^{\circ} 18' 41.94''$  (12000), in the outskirts of its host (Methods section 'The environment of SN 2023ixf within its host'). On receiving this report, we rapidly obtained a classification spectrum<sup>7</sup> at 22:23:45. The spectrum showed narrow emission lines often seen<sup>8</sup> in early-time spectra of Type II supernovae (SNe), known as flash features 9,10, including<sup>7</sup> H, He I, He II, N III, N IV, C III and C IV. We initiated a multiwavelength follow-up campaign for this event using an established methodology<sup>11</sup> (Methods sections 'Photometry', 'Spectroscopy' and 'X-ray observations'). In particular, we triggered UV spectroscopic observations using our Hubble Space Telescope (HST) target-of-opportunity (ToO) programme that proved critical to reliably track the early UV evolution of this object. Further studies of this object have been rapidly conducted and presented; a summary of these studies is provided in Methods section 'Summary of further studies of SN 2023ixf at the time of writing'.

As our HST spectra illustrate (Fig. 1), the emission from the SN peaked during the first few days in the far UV. The proximity of this event led to saturation of the UV photometers aboard the Neil Gehrels Swift Observatory, hindering standard photometric measurements. Anchoring our continuous optical-UV HST spectra to unsaturated visible-light photometry, we were able to extract reliable synthetic UV photometry

Department of Particle Physics and Astrophysics, Weizmann Institute of Science, Rehovot, Israel. 2The Oskar Klein Centre, Department of Physics, Stockholm University, AlbaNova, Stockholm, Sweden. 3 Astrophysics Research Institute, Liverpool John Moores University, Liverpool, UK. 4 The Oskar Klein Centre, Department of Astronomy, Stockholm University, AlbaNova, Stockholm, Sweden. 5Department of Astronomy, University of California, Berkeley, Berkeley, CA, USA. 6Departmento de Astrofísica, Centro de Astrobiología (CSIC-INTA), Madrid, Spain. 7School of Physics and Astronomy, Tel Aviv University, Tel Aviv, Israel. 8European Southern Observatory, Garching bei München, Germany. 9Department of Astronomy, University of Geneva, Versoix, Switzerland. 10 Physics Department and Tsinghua Center for Astrophysics (THCA), Tsinghua University, Beijing, China. 11 Université Clermont Auvergne, CNRS/IN2P3, LPC, Clermont-Ferrand, France <sup>12</sup>Department of Physics and Astronomy, Texas A&M University, College Station, TX, USA. <sup>13</sup>MIT Kavli Institute for Astrophysics and Space Research, Cambridge, MA, USA. <sup>14</sup>School of Physics, Trinity College Dublin, The University of Dublin, Dublin 2, Ireland. 15 Caltech Optical Observatories, California Institute of Technology, Pasadena, CA, USA. 16 Division of Physics, Mathematics and Astronomy, California Institute of Technology, Pasadena, CA, USA. 17The Racah Institute of Physics, The Hebrew University of Jerusalem, Jerusalem, Israel. 18Cahill Center for Astronomy and Astrophysics, California Institute of Technology, Pasadena, CA, USA. 19W. M. Keck Observatory, Kamuela, HI, USA. 20 Department of Physics and Astronomy, Northwestern University, Evanston, IL, USA. 21 Center for Interdisciplinary Exploration and Research in Astrophysics (CIERA), Northwestern University, Evanston, IL, USA. 22 Lawrence Berkeley National Laboratory, Berkeley, CA, USA. <sup>28</sup>Post Observatory, Lexington, MA, USA. <sup>24</sup>IPAC, California Institute of Technology, Pasadena, CA, USA. <sup>25</sup>Department of Astronomy, Harvard University, Cambridge, MA, USA. <sup>26</sup>Isaac Newton Group (ING), Santa Cruz de La Palma, Canary Islands, Spain. 27Department of Physics, Bar-llan University, Ramat Gan, Israel. 28Department of Astronomy & Astrophysics, University of California, San Diego, La Jolla, CA, USA. 29These authors contributed equally: E. A. Zimmerman and I. Irani. Ee-mail: erezimm@gmail.com

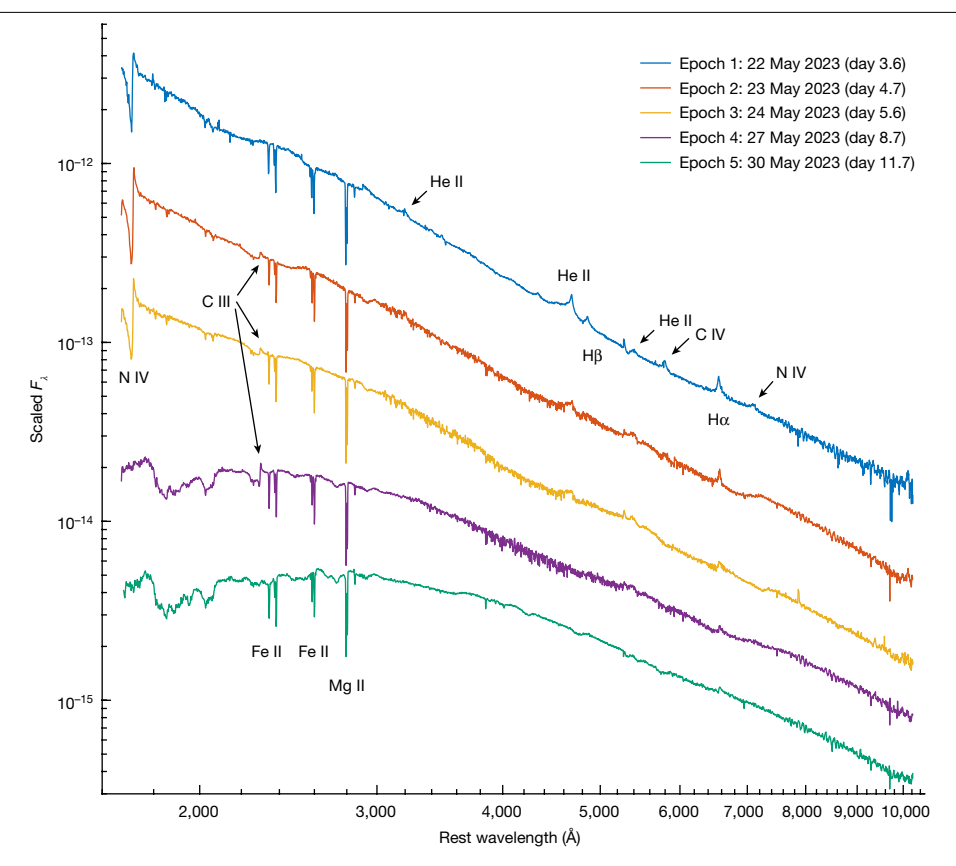


**Fig. 1**| **Early HST UV spectra of SN 2023ixf.** The spectra trace the evolving shock-ionized flash lines and reveal metal absorption lines that examine the progenitor metallicity of SN 2023ixf. All five epochs of coadded UV-optical

spectra are shown in log space to enhance the visibility of narrow features across the entire spectrum. Prominent flash features and UV absorption lines are marked, notably C III  $\lambda$ 2297 and N IV  $\lambda$ 1718.

and used it to independently confirm our custom analysis of saturated Swift observations (Methods section 'Photometry') and provide reliable UV coverage of the rise and fall of the SN light. Using the critical UV data, combined with visible-light and infrared (IR) observations (Methods section 'Photometry'), we calculate a bolometric light curve (Methods section 'Photometry') that is shown in Fig. 2, along with the derived blackbody temperature and photospheric radius.

Figure 2 shows that, during the first three days of the SN evolution, we measure an almost constant photospheric radius, with a mean value of  $(1.9 \pm 0.2) \times 10^{14}$  cm. During this phase, the temperature increases from 13,000 K to about 32,000 K at peak and the blackbody luminosity increases from  $5.2 \times 10^{42}$  erg s<sup>-1</sup> to  $3.9 \times 10^{43}$  erg s<sup>-1</sup>. For an extended shock breakout in dense CSM, the rise time is expected to be  $t_{\rm rise} = R_{\rm bo}/v_{\rm s}$  (ref. 3). Adopting the constant-radius value, we measure as the shock-breakout radius  $R_{\rm bo} = (1.9 \pm 0.2) \times 10^{14}$  cm and approximating the shock velocity  $v_{\rm s}$  by our measured photospheric velocity  $(v_{\rm s} \approx v_{\rm phot} = 8,000~{\rm km~s^{-1}}$ ; Methods section 'Spectroscopy'), we find  $t_{\rm rise} \approx 2.75 \pm 0.3$  days, in excellent agreement with the data, suggesting that the radiation-mediated explosion shock is indeed breaking out from a dense CSM distribution.

The characteristic bolometric luminosity at breakout can be estimated as the deposition of kinetic energy into the shocked CSM¹  $(L_{\rm bo} \approx M v_{\rm s}^2/t_{\rm rise})$ , in which we assume a shock velocity of 8,000 km s⁻¹ and the rise time  $t_{\rm rise}$  as the relevant duration. We can thus estimate the mass of the shocked CSM contained within the breakout radius  $R_{\rm bo}$  to be  $M \approx L_{\rm bo} t_{\rm rise}/v_{\rm s}^2 \approx (7.4 \pm 2) \times 10^{-3}~M_{\odot}$ , which suggests a characteristic density of  $\rho \approx 5 \times 10^{-13}~{\rm g~cm}^{-3}$ . Pre-explosion studies of the progenitor (Methods section 'Summary of further studies of SN 2023ixf at the time of writing') indicate that its size was much smaller¹². Assuming an expansion velocity of about 30 km s⁻¹, derived from the blueshifted centre of the narrow emission lines (Methods

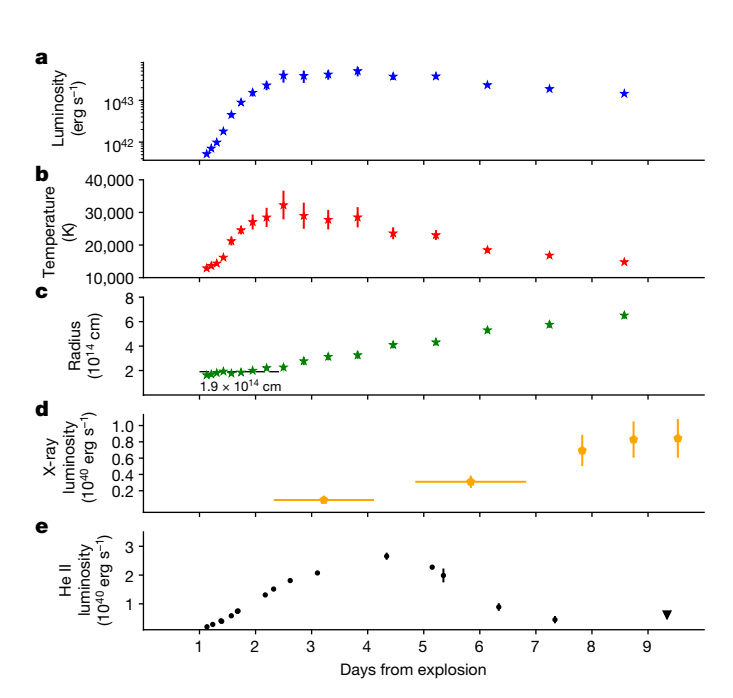


Fig. 2 | Early observables of SN 2023 ix f. a-c, The bolometric evolution of SN 2023 ix freveals the heating light curve expected from the extended breakout flare of an explosion embedded within thick CSM.  $\mathbf{d}$ ,  $\mathbf{e}$ , A rising X-ray luminosity ( $\mathbf{d}$ ) combined with high-ionization line-flux decrease (traced by He II here;  $\mathbf{e}$ ) traces the hardening of the SN SED as the explosion shock progresses into thinner CSM. All error bars show  $1\sigma$  standard deviations.

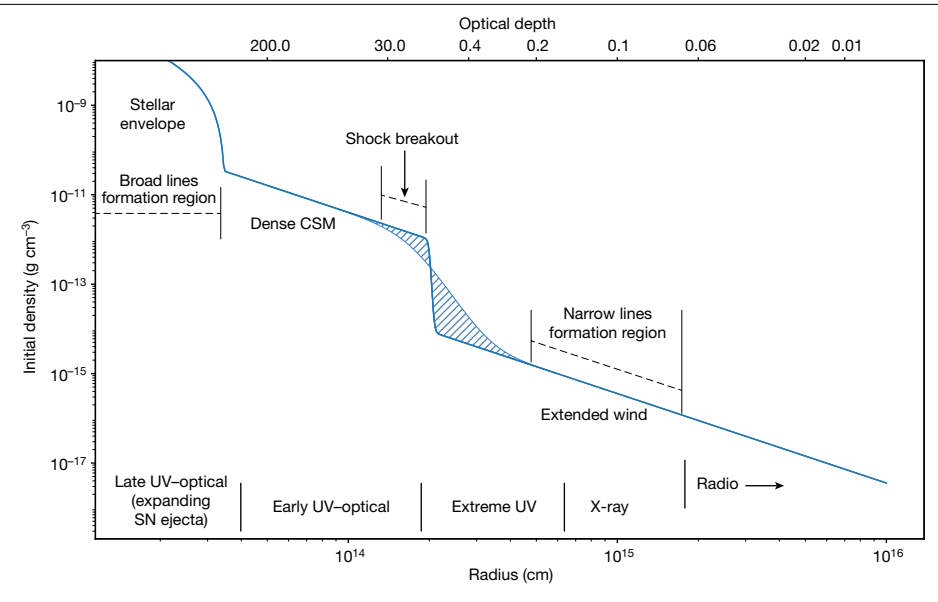


Fig. 3 | A full mapping of the CSM structure. The stellar envelope inferred from pre-explosion images extends to about  $5\times 10^{13}\,\text{cm}$  (ref. 12). Above it exists thick  $(\rho \approx 5 \times 10^{-13} \,\mathrm{g \, cm^{-3}})$  and confined  $(r \lesssim 2 \times 10^{14} \,\mathrm{cm})$  CSM, ejected shortly before the explosion, extending the shock breakout. The X-ray column-density measurements then suggest a decrease in density around the shock-breakout region into an extended wind, which could have formed throughout the RSG phase of the progenitor star. A collisionless shock forms after the decrease in

density near the shock-breakout radius, heating the CSM. At confined radii  $(R \lesssim 7 \times 10^{14} \text{ cm})$ , this heating is suppressed by Compton scattering of the SN-emitted UV-optical photons, resulting in an EUV-dominated spectrum. However, at more distant radii, Compton cooling is no longer efficient, resulting in hard X-ray bremsstrahlung emission, followed by radio synchrotron emission from the heated electrons.

section 'Spectroscopy'), we find the mass-loss rate responsible for the confined CSM to be  $\dot{M} \approx 0.011 \pm 0.005 M_{\odot} \text{ year}^{-1}$ . The velocity and mass-loss rate also match independent estimates13. At a velocity of roughly 30 km s<sup>-1</sup>, this period of enhanced progenitor mass loss could not have lasted more than a couple of years before explosion. Following the end of the extended shock breakout from the dense inner CSM, the blackbody emission radius increases rapidly and the temperature and luminosity decrease. The continued increase of the light curves in visible light (Methods section 'Photometry'; Fig. 2) is the result of the emission peak moving redward from the far UV and the growing radius.

As the shock breakout is extended, the radiation-mediated shock gradually exits the thick CSM behind the breakout region, transitioning into a collisionless shock in the CSM plasma above 14,15. This shock heats the CSM it passes through, whereas the continuously escaping photons cool the CSM electrons through inverse Compton scattering. We show this cooling process to be highly efficient (Methods section 'Evidence for shock breakout in a wind'), leading to a spectrum peaking in the extreme UV (EUV;  $\gtrsim$ 60 eV) at radii of up to  $7 \times 10^{14}$  cm. This EUV radiation is sufficient to produce the highly ionized (He II, N IV, C IV) narrow flash features appearing in the early-time spectra of SN 2023ixf, and the continuous source of ionizing photons is actually required by the total flux of lines from the ionized CSM that we see, as the integrated luminosity of narrow-line components requires each atom to be ionized many times (Methods section 'Spectroscopy'). For instance, to emit the total energy of  $(1.66 \pm 0.04) \times 10^{45}$  erg in H $\alpha$  between 1.38 and 6 days after explosion would require  $0.92 \pm 0.02 M_{\odot}$  of hydrogen if only one  $H\alpha$  photon is emitted per atom, which is ruled out by our estimate of the total CSM mass  $(M < 0.01 M_{\odot})$ .

During the initial extended shock breakout, the expanding shock in the CSM increases the EUV flux, ionizing the CSM further. This is observed through our sequence of approximately days 1–2 spectra. An increase in species ionization is seen, as N III  $\lambda\lambda$ 4634, 4641, C III  $\lambda\lambda$ 4647, 4650,  $\lambda$ 5696 and He I $\lambda$ 5876,  $\lambda$ 6678 decrease in strength and disappear, whereas higher-ionization N IV  $\lambda\lambda$ 7109, 7123, C IV  $\lambda\lambda$ 5801, 5812 and He II  $\lambda$ 4686 lines continue to increase in flux (Fig. 2).

In the UV, our HST spectra (Fig. 1) reveal two lines with P Cygni profiles developing in the near-UV (NUV). N IV  $\lambda$ 1718 with an absorption minimum at about 1,500 km s<sup>-1</sup> is apparent already in our first HST spectrum on day 3.6, and C III $\lambda$ 2297 appears on day 4.7 rapidly developing a P Cygni profile with a velocity of up to about 1,500 km s<sup>-1</sup> by day 8.7.

Apart from Ha, the optical narrow lines disappear by day 5 (Methods section 'Spectroscopy') as the shock propagates out of the efficiently Compton-cooled region, hardening the bremsstrahlung spectrum. Broad electron-scattering wings<sup>16</sup>, however, last until day 6, as they originate from scattered photons, which can be delayed by up to the dynamical size of the shock transition layer  $R_{bo}/v_s \approx 2.5$  days. The NUV N IV  $\lambda$ 1718 line disappears between days 5.5 and 8.7, consistent with the optical-line timescale, whereas the C III  $\lambda$ 2297 line persists until at least day 8.7, as it arises from a transition from an excited state populated by the EUV C III  $\lambda$ 412. The latter transition itself results from the C IV absorption of an electron into an excited C III state (a process known as dielectronic recombination)<sup>17</sup>. Thus, the persistence of this C III $\lambda$ 2297 transition reflects a parent population of excited C IV ions still ionized by the hardening X-ray flux.

By day 4 after explosion, the collisionless shock continues to propagate into further layers of CSM that are not efficiently Compton cooled. The hardening nonthermal spectrum from this lower-density CSM manifests in an escaping flux of X-rays that are detected starting on day 4 (Fig. 2). Further evidence for a sharp decrease in density is provided by a decreasing neutral hydrogen column density deduced from the Nuclear Spectroscopic Telescope Array (NuSTAR) X-ray observations<sup>18</sup>, reducing X-ray absorption. These column densities translate into a CSM density of  $4 \times 10^{-16} \, \text{g cm}^{-3}$  at a distance of  $2 \times 10^{15} \, \text{cm}$ , about three orders of magnitude below our density measurement of  $5 \times 10^{-13} \,\mathrm{g}\,\mathrm{cm}^{-3}$  at  $2 \times 10^{14} \,\mathrm{cm}$ . Figure 2 shows that the X-ray flux remains approximately constant as the collisionless shock continues to travel into the lower-density CSM. As the energy source for this emission remains the deposition of kinetic energy into shocked CSM layers  $(L \propto \dot{M}v_s^2/t = 2\pi r^2 \rho v_s^3)$ , the constant nature of the X-ray luminosity requires (for a constant velocity) a density profile falling as  $\rho \propto r^{-2}$  (Methods section 'X-ray observations'). Assuming this density profile, the

density extrapolated back to the shock-breakout radius would be  $\rho\approx 10^{-14}\,\mathrm{g}$  cm $^{-3}$ . This density is 1.5 orders of magnitude smaller than the density inferred above at the shock-breakout region, indicating a sharp density decrease (Fig. 3). Unlike the optically thick CSM below the breakout radius, this extended wind could have been produced by heightened (approximately  $10^{-4}\,M_{\odot}$  year $^{-1}$ ) $^{18}$  mass loss for decades or more before explosion (Methods section 'Photometry'). The extent of the CSM can be revealed by the duration of bright X-ray emission from SN 2023ixf. We present the full mapping of the CSM structure in Fig. 3, as inferred from the different messengers described above.

During their escape, photons interact with the CSM through radiative acceleration, dominated by the bound-free and bound-bound cross-sections (Methods section 'Radiative acceleration'). We observe this acceleration as an increase in the full width at half maximum intensity of the narrow lines, consistent with previous results<sup>19</sup>. Radiative acceleration explains the measurement of high-velocity flash features without requiring a recent stellar eruption to accelerate material to these velocities before the SN. This reconciles the SN observations with the nondetection of recent precursor eruptions from the progenitor<sup>20</sup>. The last narrow CSM spectral component surviving until day 15 is the  $H\alpha$ P Cygni profile that can be excited thermally and does not require either EUV or X-ray radiation to form. This feature disappears as the outer CSM is swept up by the ejecta on day 15, at a distance of approximately 10<sup>15</sup> cm assuming an ejecta velocity of about 8,000 km s<sup>-1</sup>. Assuming standard red supergiant (RSG) wind velocities (10-20 km s<sup>-1</sup>), this outer layer of CSM was expelled by the progenitor star a few decades before explosion. After all the narrow features subside, the SN spectrum develops typically, showing photospheric features in the optical and UV (Methods section 'Spectroscopy').

Using late-time photometric data, we calculate the <sup>56</sup>Ni mass synthe-sized by the SN explosion (Methods section 'Photometry'). Using this property, we can investigate the total mass ejected by the SN explosion<sup>21,22</sup>, given an estimate of the progenitor radius. According to the latest progenitor studies<sup>12,23</sup>, we find ejected mass estimates in the range  $M_{\rm ej}$  = 7.4 ± 0.4  $M_{\odot}$ , which are intension with a neutron star remnant with a typical mass<sup>24</sup> (1.4  $M_{\odot}$ ), given the initial masses indicated by stellar models of 12–15  $M_{\odot}$  (ref. 12) or 18.1 $_{-1.2}^{+0.7}$   $M_{\odot}$  (ref. 23). To resolve the tension, this event could have resulted in a black hole remnant. Alternatively, the progenitor needs to have lost several solar masses during its pre-explosion evolution, a behaviour not predicted by current models. A testable prediction of losing such a large mass, forming an extended CSM, is that SN 2023ixf should remain X-ray bright for years. These results highlight the ability of a combined SN and progenitor star analysis to break model degeneracies.

#### **Online content**

Any methods, additional references, Nature Portfolio reporting summaries, source data, extended data, supplementary information, acknowledgements, peer review information; details of author contributions

and competing interests; and statements of data and code availability are available at https://doi.org/10.1038/s41586-024-07116-6.

- Waxman, E. & Katz, B. in Handbook of Supernovae (eds Alsabti, A. & Murdin, P.) 967-1015 (Springer, 2017).
- Bersten, M. C. et al. A surge of light at the birth of a supernova. Nature 554, 497–499 (2018)
- Ofek, E. O. et al. Supernova PTF 09UJ: a possible shock breakout from a dense circumstellar wind. Astrophys. J. 724, 1396 (2010).
- Garnavich, P. M. et al. Shock breakout and early light curves of type II-P supernovae observed with Kepler. Astrophys. J. 820, 23 (2016).
- Riess, A. G. et al. A comprehensive measurement of the local value of the Hubble constant with 1 km s<sup>-1</sup> Mpc<sup>-1</sup> uncertainty from the Hubble Space Telescope and the SHOES team. Astrophys. J. Lett. 934, L7 (2022).
- 6. Itagaki, K. Transient Discovery Report for 2023-05-20. Transient Name Server (2023).
- Perley, D. A. et al. LT classification of SN 2023ixf as a Type II supernova in M101. Transient Name Server AstroNote 2023-119 (2023).
- Bruch, R. J. et al. The prevalence and influence of circumstellar material around hydrogen-rich supernova progenitors. Astrophys. J. 952, 119 (2023).
- Gal-Yam, A. et al. A Wolf-Rayet-like progenitor of SN 2013cu from spectral observations of a stellar wind. Nature 509, 471-474 (2014).
- Yaron, O. et al. Confined dense circumstellar material surrounding a regular type II supernova. Nat. Phys. 13, 510–517 (2017).
- Gal-Yam, A. et al. Real-time detection and rapid multiwavelength follow-up observations
  of a highly subluminous Type II-P supernova from the Palomar Transient Factory survey.
  Astrophys. J. 736, 159 (2011).
- Van Dyk, S. D. et al. The SN 2023ixf progenitor in M101: II. Properties. Preprint at https://arxiv.org/abs/2308.14844 (2023).
- Jacobson-Galán, W. V. et al. SN 2023ixf in Messier 101: photo-ionization of dense, close-in circumstellar material in a nearby type II supernova. Astrophys. J. Lett. 954, 142 (2023).
- Katz, B., Sapir, N. & Waxman, E. in Death of Massive Stars: Supernovae and Gamma-Ray Bursts (eds Roming, P., Kawai, N. & Pian, E.) 274–281 (2012).
- Margalit, B., Quataert, E. & Ho, A. Y. Q. Optical to X-ray signatures of dense circumstellar interaction in core-collapse supernovae. Astrophys. J. 928, 122 (2022).
- Huang, C. & Chevalier, R. A. Electron scattering wings on lines in interacting supernovae. Mon. Not. R. Astron. Soc. 475, 1261–1273 (2018).
- Hillier, D. J. Photoionization and electron-ion recombination in astrophysical plasmas.

  Atoms 11 54 (2023)
- Grefenstette, B. W., Brightman, M., Earnshaw, H. P., Harrison, F. A., & Margutti, R. Early hard X-rays from the nearby core-collapse supernova SN 2023ixf. Astrophys. J. Lett. 952, 13 (2023)
- Smith, N. et al. High-resolution spectroscopy of SN 2023ixf's first week: engulfing the asymmetric circumstellar material. Astrophys. J. 956, 46 (2023).
- Dong, Y. et al. A comprehensive optical search for pre-explosion outbursts from the quiescent progenitor of SN 2023ixf. Astrophys. J. 957, 28 (2023).
- Shussman, T., Nakar, E., Waldman, R. & Katz, B. Type II supernovae progenitor and ejecta
  properties from the total emitted light, ET. Preprint at https://arxiv.org/abs/1602.02774
  (2016).
- Nakar, E., Poznanski, D. & Katz, B. The importance of <sup>5</sup>6Ni in shaping the light curves of type II supernovae. Astrophys. J. 823, 127 (2016).
- Qin, Y.-J. et al. The progenitor star of SN 2023ixf: a massive red supergiant with enhanced, episodic pre-supernova mass loss. Preprint at https://arxiv.org/abs/2309.10022 (2023).
- Özel, F., Psaltis, D., Narayan, R. & Villarreal, A. S. On the mass distribution and birth masses of neutron stars. Astrophys. J. 757, 55 (2012).

**Publisher's note** Springer Nature remains neutral with regard to jurisdictional claims in published maps and institutional affiliations.

Springer Nature or its licensor (e.g. a society or other partner) holds exclusive rights to this article under a publishing agreement with the author(s) or other rightsholder(s); author self-archiving of the accepted manuscript version of this article is solely governed by the terms of such publishing agreement and applicable law.

@ The Author(s), under exclusive licence to Springer Nature Limited 2024

### Methods

#### The environment of SN 2023ixf within its host

The SN 2023ixf explosion site is located 9 kpc from the centre of M101 (redshift z = 0.00084)<sup>25</sup> on the far side of an outer spiral arm (Extended Data Fig. 1). This region of the host galaxy is a site of continuing star formation, with islands of enhanced star formation and diffusely distributed lower-level star-formation activity extending to the SN site (Extended Data Fig. 1c).

#### **Photometry**

All phases in this manuscript refer to JD = 2,460,083.3 as the SN explosion time, as inferred from early analysis of amateur-astronomer pre-explosion observations of M101 (ref. 26).

We obtained a full multiband light curve of SN 2023ixf, covering the early increase, plateau and radioactive decline. We present the full light curve in Extended Data Fig. 2. The data are available from the WISeREP database. Standard reduction procedures are described in the Supplementary information, as are our methods for reduction of saturated Swift photometry using the streak photometry method<sup>27</sup>.

<sup>56</sup>Ni mass and ejected mass estimate. By t = 90 days, the light curve has fully settled onto the radioactive <sup>56</sup>Co tail. The <sup>56</sup>Ni mass can be directly estimated from the bolometric luminosity<sup>28,29</sup>, which is equal to the energy deposition from <sup>56</sup>Co decay, assuming full trapping of y-ray photons, as is typical for SNe II at this phase<sup>30</sup>. We calculate bolometric corrections at late times using spectra of SN 2017ahn (ref. 31), which shows similar persistent narrow features<sup>32</sup> and peak luminosity, although a slightly shorter plateau duration. We stitch together nebular spectra of SN 2017ahn obtained after the fall from the plateau in the optical (t = 72 days) and IR (t = 65 days) to match each other. We then calculate the bolometric correction to the uBgriz photometry from the combined spectrum, extended assuming a blackbody extrapolation outside the observed band. This estimate is within 15% of the bolometric luminosity calculated directly using a blackbody extrapolation to the SN 2023ixf uBgriz photometry. We find that the bolometric light curve of SN 2023ixf is well described by the energy deposition from a <sup>56</sup>Ni mass of  $M_{56_{\text{Ni}}} = 0.071 \pm 0.005 \, M_{\odot}$ . A 5% systematic error is included to account for the scatter in the IR contribution (>9,000 Å) to the bolometric flux at t = 90 days (ref. 33). Our estimate places SN 2023ixf at the upper end of the Type II <sup>56</sup>Ni mass distribution<sup>29</sup>. We show the full bolometric light curve, bolometric correction and <sup>56</sup>Ni deposition in Extended Data Fig. 3.

Using the bolometric luminosity and the deposition from  $^{56}$ Ni, we calculate the time-weighted integrated bolometric luminosity ET =  $\int Lt dt - \int Q_{56_{\text{Ni}}}t dt$ , in which  $Q_{56_{\text{Ni}}}$  is the deposition from  $^{56}$ Ni. We note that ET =  $0.1 M_{\rm ej} R. v_{\rm ej}$  is directly related to the ejected mass  $M_{\rm ej}$ , progenitor radius R. and typical velocity  $v_{\rm ej}$ ; it is dependent only on the hydrodynamical profiles and is insensitive to the exact details of radiation transport and CSM mass<sup>21,22</sup>; our result is ET =  $(3.3 \pm 0.2) \times 10^{55}$  erg s<sup>-1</sup>. The bulk ejecta velocity is estimated<sup>22</sup> from the  $\lambda$ 5169 Fe II line  $v_{\rm ej} = v_{\lambda$ 5169,50days</sub> = 3,400 ± 200 km s<sup>-1</sup> and we use four recent estimates existing for the progenitor radius from pre-explosion data<sup>12,23,34,35</sup>. We derive the radius from the effective temperature and luminosity of the progenitor using  $R = (L/(4\pi\sigma T_{\rm eff}^{-1}))^{1/2}$ . Our constraints on the ejected and remnant masses are presented in Supplementary Table 1.

Combining the constraint of two recent studies  $^{12,23}$  gives an ejected mass of  $7.4 \pm 0.4 \, M_{\odot}$ . We note that the calculated ejected mass for one study  $^{35}$  leaves a negative remnant mass, creating a tension between the ejected mass estimate from the SN properties and their initial mass estimate. To reconcile the initial mass implied by the other studies  $^{12,23,34}$  with the ejected-mass estimate, the progenitor probably had to either lose a large fraction of its mass before explosion or leave a black hole remnant. The former option requires that the mass-loss rate of about  $10^{-4} \, M_{\odot}$  year  $^{-1}$  inferred from the CSM extended wind would persist for

 $10^4$ – $10^5$  years, much or most of the red-supergiant phase of the progenitor star. In such a case, because X-ray examines the extent of the CSM extended wind through the shock velocity, the SN will continue to be X-ray bright for years.

#### Spectroscopy

We obtained a total of 112 spectra of SN 2023ixf. Details the instruments and configurations of these spectra is given in the Supplementary information. The sequence of spectra in different phases is shown in Extended Data Figs. 4, 5 and 7. All reduction notes are available in the Supplementary information.

**HST.** Immediately following the classification of SN 2023ixf as a Type II event showing flash-ionization features , less than 90 min from the SN discovery, we initiated our disruptive HST programme GO-17205 (PIE. Zimmerman) as part of the follow-up campaign. Rapid response and observation scheduling resulted in the first epoch of HST spectroscopy being obtained <50 h after the SN discovery, providing the first ever NUV spectrum of a Type II SN during the flash-feature phase. Furthermore, as photometry from Swift saturated after t=2 days, the HST spectra were the only reliable source of UV information by providing synthetic UV photometry. This synthetic photometry validated the readout-streak Swift photometry reduction and, thus, was the basis of the entire SN UV light curve.

Five visits of SN 2023ixf were carried out as planned, covering a total of 22 HST orbits. All visits in the programme were weighted towards the NUV, obtaining several orbits with the G230LB grism, but also included coverage of the optical part of the spectrum with single-orbit exposures using the G430L and G750L grisms. A full list of the programme HST visits and exposures is shown in the Supplementary information. Our sequence of HST spectra is presented in Fig. 1, showing a coadded spectrum for each of our five HST programme visits. Reduction notes for the HST spectra are presented in the Supplementary information.

The most notable CSM features in the UV spectra are the N IV  $\lambda$ 1718 and C III  $\lambda$ 2297 P Cygni profiles, with high velocities of >2,500 km s<sup>-1</sup> (Supplementary Fig. 2). Along with the strong N IV and C III emission lines in the UV spectra, we find prominent line-of-sight absorption lines of Fe II and Mg II, as well as weaker Al III, Zn II, Mn II and Cr II (seen in Fig. 1). These are known interstellar medium lines<sup>36</sup> and are accompanied by absorption lines of Ca and Na seen in high-resolution optical spectra from the High Accuracy Radial Velocity Planet Searcher for the Northern Hemisphere (HARPS-N). These absorption features also appear in spectra of other Type II SNe (see Extended Data Fig. 6), but they are stronger in SN 2023ixf.

In Extended Data Fig. 6, we compare the photospheric features of SN 2023ixf to other early-time UV spectra of Type II SNe. The UV photospheric features of SN 2023ixf show a resemblance to those appearing in the early UV spectra of SN 2022wsp (ref. 37), SN 2021yja (ref. 38) and SN 2022acko (ref. 39), suggesting some uniformity among Type II-P SNe. On the other hand, the photospheric features of SN 2023ixf develop later than in SN 2022acko, for which we have early-time NUV spectra, and lack a strong emission feature at approximately 1,910 Å appearing in the early NUV spectra of SN 1999em (ref. 40) and SN 2005ay (ref. 41). To assess the diversity of Type II SN NUV photospheric spectra, a larger sample of early-time NUV spectra must be collected. As some uniformity is observed in at least four recent SNe, these photospheric features must arise from the progenitor natal chemical composition and not from species synthesized during the SN explosion itself, whose parameters differ among explosions. It would thus be very informative to examine the progenitor chemical composition by modelling these early-time NUV spectra.

**Shock velocity.** To estimate the shock velocity of SN 2023ixf, we adopt the blue-edge velocity of the broad photospheric H $\alpha$ P Cygni profile.

This velocity is reminiscent of the shock front as it represents the fastest bulk material heading towards the observers. The photospheric velocity has been shown to represent the shock velocity in cases in which the mass-loss rate is lower than  $10^{-2} M_{\odot} \, \text{year}^{-1}$  in theoretical work<sup>42</sup>. We show this velocity to be  $v_s \approx 8,000 \, \text{km s}^{-1}$  in Extended Data Fig. 7.

**Narrow-line velocities.** Using our sequence of high-resolution (R = 45,000) NOT/FIES spectra, we measure the velocities of the fully resolved strongest narrow flash features, namely, H $\alpha$ , H $\beta$ , He II $\lambda$ 4686, C IV  $\lambda\lambda$ 5801, 5812 and N IV  $\lambda\lambda$ 7109, 7123. For the Balmer lines, we also measure the corresponding He II  $n \rightarrow 4$  transition velocity. Our velocity measurements are presented in Supplementary Table 2.

Depending on the epoch, we fit different phenomenological models to the narrow features to measure the velocity of different spectral components. To remove the local continuum, we fit a third-degree polynomial to the continuum (masking the line) and divide the spectrum by it. For the t=2.23 days spectrum, we fit a model consisting of a Lorentzian base (representing the electron-scattering wing) with Gaussian components representing the narrow lines themselves. For He II  $\lambda$ 4686, a blueshifted Lorentzian base is added, improving our overall fit to this line. We interpret this blue excess as originating from the scattering caused by the (by this epoch) ionized N III  $\lambda$ 4640, which we have shown can be delayed by up to  $t_{bo}$  in evolution. Overall, we find all narrow lines to be consistent with velocities of about 100 km s<sup>-1</sup> at this epoch. All narrow lines are shifted blueward by roughly 30 km s<sup>-1</sup>, except for H $\alpha$ , which may be contaminated by M101 emission. These fits are shown in Supplementary Fig. 1.

No clear narrow components are visible for the t = 4.3 and 5.11 days spectra. Therefore, we fit Lorentzian profiles to the flash features (except for He II  $\lambda$ 4686 at t = 4.3 days, for which a narrow Gaussian component is added to the fit as well). Starting from t = 8.13 days, as no other narrow features appear in the optical spectra, we only fit a model to Hα, showing a narrow P Cygni profile. This profile is represented with a redshifted Lorentzian emission component adjacent to a blueshifted Gaussian absorption component. To avoid introducing a saddle mimicking the absorption component, we use a first-degree polynomial to remove the continuum from these later spectra. These fits are presented as Supplementary Fig. 2. We define the P Cygni velocity to be three times the standard deviation of the Gaussian absorption component. This corresponds to the absorption profile blue edge well in cases in which this edge is clear and can also be measured when uncertain continuum levels hinder the blue-edge measurement. A velocity of  $v \approx 2,000 \text{ km s}^{-1}$  is inferred from the mean of all four epochs. All fits were made using the Imfit package<sup>43</sup>.

**Narrow-line fluxes.** To investigate the strength of the narrow lines, we measure their flux using the sequence of medium-resolution spectra. To do so, we fit a first-degree polynomial to the continuum in the emission-line vicinity and remove it from the spectrum. We define the borders of the nearby continuum by drawing its edge from a uniform distribution. The emission flux is then obtained using trapezoidal integration. We repeat this process 1,000 times, drawing different edges to the continuum, and take the mean value as the measurement and the standard deviation as the measurement uncertainty.

The total emitted flux from He II and H $\alpha$  cannot be explained by a single ionization event, as it corresponds to the emission of one photon per atom by about  $1M_{\odot}$  of material. We present He II flux measurements in Fig. 2 and the other line fluxes in the Supplementary information.

**Extinction estimate.** To examine the host-galaxy extinction, we adopt established relations<sup>44</sup> between the equivalent width of Na I D absorption and extinction. We use our sequence of spectra from the HARPS-N, which resolves the Na absorption completely. The equivalent width is measured directly from the spectra after removing any microtelluric absorption, taking the mean of the first HARPS-N spectra (for

which we measure no decrease in Na component equivalent width). The equivalent-width measurements are shown in Supplementary Table 3. We determine E(B - V) = 0.034 mag, which we multiply by a factor of 0.86 to correct for dust recalibration<sup>45</sup>; the final result is  $E(B - V) = 0.029 \pm 0.005$  mag. Systematics dominate the uncertainty.

#### X-ray observations

The Swift satellite obtained several observations of SN 2023ixf at X-ray energies with its X-ray telescope (XRT)<sup>46</sup> in photon-counting mode. We present the early X-ray increase in Fig. 2 and the full X-ray light curve is shown in Extended Data Fig. 8. The individual measurements are summarized in Supplementary Table 4. After an initial increase in the X-rays, SN 2023ixf settles onto an X-ray plateau. As the luminosity of a cooling forward shock is given by  $L = 2\pi r^2 \rho v_{\rm sh}^3$  and the shock velocity  $v_{\rm sh}$  is only slowly decreasing (that is, staying roughly constant at early times), a constant X-ray light curve suggests a steady mass loss and a density profile  $\rho \propto r^{-2}$ , in which r is the distance from the progenitor star. We note that, at the time of writing, SN 2023ixf is still X-ray bright. Detailed-reduction notes of the XRT data are shown in the Supplementary information.

## Summary of further studies of SN 2023ixf at the time of writing

Located in the nearby, well-known galaxy M101, SN 2023ixf attracted notable attention from the community. In this section, we summarize the main results published thus far.

Studies of the narrow lines. Several papers have discussed the early-time optical flash features and their temporal progression<sup>13,47</sup>. These studies present early flash spectroscopy of SN 2023ixf and discuss the increase in the flash-feature ionization (He I, N III, C III → He II, N IV, C IV), unique to this event. Both studies also compare the early spectra to non-local-thermodynamic-equilibrium models, reaching a mass-loss-rate estimate on the same order of magnitude as that inferred by us for the confined CSM up to the shock-breakout radius of  $\dot{M} \approx 2 \times 10^{-2} M_{\odot}$  year<sup>-1</sup>. One study<sup>13</sup> finds a density of  $\rho \approx 10^{-12}$  g cm<sup>-3</sup> at a radius of  $r \approx 10^{14}$  cm, consistent with our results. Both studies suggest that the CSM is confined to  $(0.5-1.0) \times 10^{15}$  cm. We find that low-density CSM extends further to explain the persistent X-ray luminosity and narrow spectroscopic features until at least day 8.7 (C III  $\lambda$ 2297) and day 15 (H $\alpha$ ). A comparison with a radiative-transfer model (r1w6b)<sup>48</sup> is presented in one study as well<sup>13</sup>, extending to the UV. Both studies also compare SN 2023ixf to other SNe showing flash features and note the similarity of SN 2023ixf to SN 1998S (refs. 49,50), SN 2017ahn (ref. 31), SN 2020pni (ref. 51) and SN 2020tlf (ref. 52), all of which show long-lasting flash features compared with most other SNe (ref. 8). We also note that SN 2017ahn, SN 2020pni and SN 2020tlf all exhibit an increase in their bolometric luminosity, suggesting that they experience an extended shock breakout in a wind, similar to SN 2023ixf.

Detailed high-resolution spectroscopy of the narrow lines was presented in another study <sup>19</sup>. This showed that the narrow lines exhibit broadening between days 2 and 4. Our high-resolution velocity measurements from t=2.3 days are consistent with this result, and the broadening of narrow lines is consistent with our results on radiative acceleration of the CSM. We add the velocity measurements by this study into Extended Data Fig. 9. This work also discusses the possibility of the CSM being asymmetric, citing the difference in blueshift between highly ionized species and lack of narrow (approximately  $100 \text{ km s}^{-1}$ ) P Cygni profiles. In our independent analysis, we also observe a blueshift of the narrow lines in the t=2.3-day NOT/FIES spectrum (see Supplementary Fig. 1 and Supplementary Table 2). We note, however, that UV spectroscopy reveals deep, narrow P Cygni profiles, unlike the optical H $\alpha$  profile.

**Spectropolarimetry.** Early-time spectropolarimetry of SN 2023ixf was obtained<sup>53</sup>, which observes a high continuum polarization of  $p_{\rm cont} \approx 1\%$  until day 2.5, reducing to 0.5% on day 3.5 after explosion. This timeline

is consistent with our extended shock-breakout time  $R_{bo}/v_s \approx 2.5$  days. As discussed in that study<sup>53</sup>, as the shock moves within optically thick CSM, the photosphere is expected to originate from a radius at which the optical thickness  $\tau \approx 2/3$ . This is consistent with the roughly constant radius obtained through our blackbody measurements, suggesting that, at this radius (about  $1.9 \times 10^{14}$  cm), the CSM is aspherical. We note, however, that this asymmetry is only measured in layers above the breakout radius. The sudden change in polarization between days 2.5 and 3.5 is also consistent with a change in the CSM structure, which coincides with the reduction in density that we derive as the SN shock moves from the confined CSM into the extended wind (with the measurement of first X-ray emission). The study also observes a depolarization in the centre of the narrow He II  $\lambda$ 4686 and H $\alpha$  emission<sup>53</sup>, suggesting that they form above the early polarized photosphere. This is consistent with our results, showing that many of the narrow features form in the extended wind.

**X-ray and other messengers.** As demonstrated through our CSM model, X-ray and (mostly lack of) radio detections of SN 2023ixf have been critical messengers in the mapping of CSM structure.

Two epochs of X-ray observations with the NuSTAR were previously obtained  $^{18}$ . Although both epochs are covered by the Swift/XRT as well, NuSTAR provides several important insights unavailable through XRT. Both epochs fit a bremsstrahlung spectrum, with a peak at >25 and  $34_{-12}^{+22}$  keV, respectively, showing that the X-ray spectrum is hard. The inferred NuSTAR unabsorbed bolometric X-ray luminosity in both epochs of  $L_{\rm X}\approx 2.5\times 10^{40}~{\rm erg~s^{-1}}$  is consistent with our XRT measurements, taking into account a bolometric correction. Last, the decrease in soft X-ray absorption between the first NuSTAR epoch (about 4 days) and the second epoch (about 11 days) traces the extended-wind profile and is consistent with the decrease in density we expect after the shock-breakout region. We adopt the mass-loss rate and densities reported by this study as the extended-wind density.

Limits on millimetre observations of SN 2023ixf were reported as well<sup>54</sup>, which are consistent with the high mass-loss rate we infer for the confined CSM, but inconsistent with the lower mass-loss rates we infer for the extended wind. NuSTAR data, however, show that lower mass-loss rates consistent with our extended-wind model can also be allowed by the radio data for the extended wind<sup>18</sup>.

**Photometric evolution and models.** A fit to a recent shock-cooling model<sup>55</sup> for photometry starting at t=1 day was shown in another study<sup>56</sup>. As we measure the SN heating for the first 2.5 days, we find this result to be inconsistent with our data. Although shock cooling can describe the unsaturated early-time Swift/UVOT photometry, it is in conflict with the full SN light curve, including our HST data and Swift streak photometry, which shows a prolonged increase in all UV bands. This study also discusses a change in the light-curve behaviour between the first day before discovery by Itagaki and later photometry. This is consistent with our pre-discovery P48 g-band photometry. Further discussion of the change in slope between very early times and the +1-day light curve will be presented in a future paper analysing more amateur-astronomer photometry (O.Y. et al., manuscript in preparation).

Blackbody spectral energy distribution (SED) fits to the UBVRI light curve (that is, excluding the saturated Swift data) were performed in another study  $^{57}$ , reaching the conclusion that SN 2023ixf experiences heating during the first roughly 5 days after explosion. That study therefore concludes that the SN goes through an extended shock breakout in a wind, consistent with our results. However, owing to the inaccessibility of the saturated UV light curve, the bolometric luminosity is only sampled in the Rayleigh–Jeans regime, causing an overestimation of the luminosity rise time (by about 2.5 days) and an underestimation of the SN heating (by about 16,000 K). Therefore, this leads to the conclusion that the confined CSM extends much farther than our results ((3–7) ×  $10^{14}$  cm compared with approximately  $2 \times 10^{14}$  cm).

A multiband study of SN 2023ixf (ref. 58) presented the Swift grism NUV observations and three epochs of photospheric (starting from +6.9 days) FUV spectra using the Ultraviolet Imaging Telescope (UVIT) aboard the AstroSat satellite. The study also performed a light-curve investigation without the saturated early-time UV data, inferring a more extended dense CSM than our results.

**Progenitor properties.** Several studies have pointed out a candidate progenitor star using pre-explosion images<sup>12,23,34,35,59</sup>, indicating that the progenitor candidate was a RSG experiencing periodic (about 1,000 days) mass-loss episodes. Constraints on the mass-loss parameters from the progenitor IR variability and SED fits were given in several studies<sup>23,34,59</sup>. This mass loss should reflect the extended wind, as the confined CSM must have been ejected closer to the time of explosion owing to its much larger density. The inferred CSM densities from these studies are indeed consistent with the values we measure for the extended wind. However, it is interesting to note that no eruptive source has been identified for the confined CSM (below the breakout radius) in optical<sup>20</sup>, UV (ref. 60) or IR observations<sup>34</sup>. The IR data were obtained merely 10 days before the explosion.

#### Evidence for shock breakout in a wind

**Blackbody fits.** Starting at the first time when multiband photometry is available at JD = 2,460,084.42, we linearly interpolate our photometry onto a grid with uniform steps in log time. For each grid point, we fit the resulting SED with a blackbody function to recover the blackbody bolometric luminosity, radius and temperature of SN 2023ixf. We also compare the optical–UV HST spectra to a grid of blackbody temperatures and luminosities and calculate the best fit and the corresponding uncertainties, assuming a likelihood  $\log L \approx \chi^2$ . Both methods are in good agreement. We show these fits in Supplementary Fig. 3 and the fit results are shown in the Supplementary information. A full bolometric light curve is shown in Extended Data Fig. 3.

Compton cooling of the shock-heated wind at early times. As the radiation-mediated shock breaks out of the dense CSM, the accelerated ejecta hit the low-density and optically thin wind, creating a collisionless shock<sup>1,14</sup> that is mediated by collective plasma instabilities. The average proton temperature at the shocked region  $^{14,15}$  is  $T_p \approx 0.2$  MeV. The electrons are heated by the shock passage and Coulomb interactions with the protons to temperatures of ≥60 keV. These energetic electrons inverse-Compton scatter on the flux of UV photons from the underlying breakout region, suppressing the X-ray flux at early times. Owing to the large density difference between the breakout region and the extended encompassing wind, there are not enough hot electrons to affect the UV-optical spectral peak substantially. Rather, the plasma energy is carried away by EUV photons created through inverse-Compton scattering. The spectrum will continuously harden as the radiation flux decreases with time and distance, making this cooling channel inefficient.

The cooling rate of a plasma with energy  $E_p$  of hot electrons at  $\tau < 1$  and at a temperature T by photons at much lower energies is given by

$$dE_p = -\frac{\sigma_T}{4\pi r^2} \frac{4TL_{\gamma} dt}{m_c c^2},$$
 (1)

in which  $\sigma_T$  is the Thompson cross-section and  $m_e c^2$  is the electron rest-mass energy. Assuming  $E_p = 3T$ , we find

$$\frac{\mathrm{dlog}E_{\mathrm{p}}}{\mathrm{d}t} = -\frac{\sigma_{\mathrm{T}}}{3\pi r^{2}} \frac{L_{\gamma}}{m_{\mathrm{e}}c^{2}}.$$
 (2)

Using the observed bolometric light curve, we calculate the cooling rate of the plasma by the breakout burst photons at various locations and times since the explosion. We show these results in Supplementary

Fig. 4; they indicate that, during the first day of the explosion, Compton cooling is not yet substantial enough to prevent X-ray emission, but no observations exist at this time. During days t=2-6, X-ray emission is suppressed at the collisionless shock front, but the electrons remain hot enough to allow EUV emission. After day 6, the density decreases and X-ray emission is no longer suppressed by inverse-Compton scattering. Our results are broadly consistent with the observed He II emission (ionized efficiently by  $\lesssim\!100\text{-eV}$  photons) before day 6 and the emergence of X-rays on days 4–5. The continued presence of C III  $\lambda2297$  after the disappearance of He II is consistent with the hardening of the illuminating spectrum rather than an effect of recombination time.

#### Radiative acceleration

Radiative acceleration of CSM has been calculated <sup>61</sup> and shown to have occurred in previous SNe, such as SN 2010jl (ref. 62), which—as a Type IIn SN—showed notable interaction with its CSM environment. Here we calculate the velocity gained by radiative acceleration at a given radius using the time-dependent blackbody spectral luminosity that we measured (Methods section 'Photometry') for SN 2023ixf.

The acceleration a spherical shell of material at  $\tau < 1$  experiences owing to a flux  $f_v$  passing through it is given by

$$\frac{\mathrm{d}^2 r}{\mathrm{d}t^2} = \frac{1}{4\pi r^2 \mu c} \int_0^\infty L_\nu \sigma_\nu \mathrm{d}\nu,\tag{3}$$

in which  $L_{\nu}$  is the spectral luminosity of the internal source,  $\mu = 0.7 m_{\rm p}$ is the average particle mass assuming solar mixture and  $\sigma_{\nu}$  is the total cross-section at a given frequency. To estimate the total cross-section, we use an open-source opacity table<sup>55</sup> based on atomic line lists<sup>63</sup> by assuming CSM with a density of  $10^{-15}$  g cm<sup>-3</sup> and a temperature of 5 eV, which would generate a thermal-electron-velocity distribution consistent with the full width at half maximum of the electron-scattering wings of the narrow emission lines observed during the first few days. The effective cross-section owing to bound-bound and bound-free processes dominates the effective cross-section for acceleration (but not for diffusion) and is much larger than the Thompson cross-section. Although the CSM is not in local thermodynamic equilibrium with the incoming radiation from the underlying SN, the cross-section is most affected by bound-free interactions in the plasma. A full steady-state solution of the fractions of different plasma species is outside the scope of this work.

In Extended Data Fig. 9, we show the velocities measured from various narrow lines as they evolve until photospheric features emerge. Our calculation demonstrates that, with a fraction of neutral elements achieved at 5 eV, the absorption cross-section is sufficiently high to fully  $explain \, the \, observed \, line \, velocities \, with \, radiative \, acceleration \, from \, the \,$ SN UV-optical emission at a single location. The first high-resolution spectrum capable of resolving lines with  $v < 100 \text{ km s}^{-1}$  was taken at t = 2.3 days. At this time, radiative acceleration was already high enough to dominate the observed velocity, indicating that the CSM velocity is not measured from these features. As a consequence of our calculation, we also determine the position and radiative acceleration experienced by shells immediately above the breakout region. Given sufficient time, matter below the shock-breakout region (instead of the ejecta) would accelerate enough to shock the matter. In our case, notable acceleration does not occur before day 3. By this time, the ejecta themselves will sweep up all matter, which can be accelerated to >5,000 km s<sup>-1</sup>, indicating that a collisionless shock had, in fact, formed above the breakout region.

#### **Data availability**

Photometry and spectra used in this study will be made available from WISeREP<sup>64</sup> (http://wiserep.weizmann.ac.il/). A log of the available spectra can be found in the Supplementary information. Other

source data files are available in the Supplementary information and Excel sheets. OPTICON observations were obtained under programme ID OPT/2023A/001. PLE. Zimmerman.

## **Code availability**

Relevant software sources and web locations have been provided in the text and are publicly available. All scripts used to conduct the analyses presented in this paper are available from the corresponding author on request.

- 25. de Vaucouleurs, G. et al. Third Reference Catalogue of Bright Galaxies (Springer, 1991).
- Yaron, O. et al. Amateur astronomer contribution to constraining the explosion time and rise of the Type II SN 2023ixf in M101. Transient Name Server AstroNote 2023-133 (2023).
- Page, M. J. et al. The use and calibration of read-out streaks to increase the dynamic range of the Swift Ultraviolet/Optical Telescope. Mon. Not. R. Astron. Soc. 436, 1684–1693 (2013)
- Bersten, M. C., & Hamuy, M. Bolometric light curves for 33 Type II plateau supernovae. Astrophys. J. 701, 200 (2009).
- Valenti, S. et al. The diversity of Type II supernova versus the similarity in their progenitors. Mon. Not. R. Astron. Soc. 459, 3939–3962 (2016).
- Sharon, A., & Kushnir, D. The γ-ray deposition histories of core-collapse supernovae. Mon. Not. R. Astron. Soc. 496, 4517–4545 (2020).
- Tartaglia, L. et al. The early discovery of SN 2017ahn: signatures of persistent interaction in a fast-declining Type II supernova. Astrophys. J. 907, 52 (2021).
- Yamanaka, M., Fujii, M. & Nagayama, T. Bright Type II supernova 2023ixf in M 101: a quick analysis of the early-stage spectra and near-infrared light curves. *Publ. Astron. Soc. Jpn.* 75, L27–L31 (2023).
- Lyman, J. D., Bersier, D. & James, P. A. Bolometric corrections for optical light curves of core-collapse supernovae. Mon. Not. R. Astron. Soc. 437, 3848–3862 (2014).
- Jencson, J. E. et al. A luminous red supergiant and dusty long-period variable progenitor for SN 2023ixf. Astrophys. J. Lett. 952, L30 (2023).
- Kilpatrick, C. D. et al. SN 2023ixf in Messier 101: a variable red supergiant as the progenitor candidate to a type II supernova. Astrophys. J. Lett. 952, L23 (2023).
- Morton, D. C. Atomic data for resonance absorption lines. III. Wavelengths longward of the Lyman limit for the elements hydrogen to gallium. Astrophys. J. Suppl. Ser. 149, 205 (2003).
- Vasylyev, S. S. et al. Early-time ultraviolet and optical Hubble Space Telescope spectroscopy of the Type II supernova 2022wsp. Astrophys. J. Lett. 959, L26 (2023).
- Vasylyev, S. S. et al. Early-time ultraviolet spectroscopy and optical follow-up observations of the Type IIP supernova 2021yja. Astrophys. J. 934, 134 (2022).
- Bostroem, K. A. et al. SN 2022acko: the first early far-ultraviolet spectra of a Type IIP supernova. Astrophys. J. Lett. 953, L18 (2023).
- Baron, E. et al. Preliminary spectral analysis of the Type II supernova 1999EM. Astrophys. J. 545, 444 (2000).
- Gal-Yam, A. et al. GALEX spectroscopy of SN 2005ay suggests ultraviolet spectral uniformity among Type II-P supernovae. Astrophys. J. 685, L117 (2008).
- Moriya, T. J., Förster, F., Yoon, S.-C., Gräfener, G. & Blinnikov, S. I. Type IIP supernova light curves affected by the acceleration of red supergiant winds. Mon. Not. R. Astron. Soc. 476, 2840–2851 (2018).
- Newville, M., Stensitzki, T., Allen, D. B. & Ingargiola, A. LMFIT: non-linear least-square minimization and curve-fitting for Python. Zenodo https://zenodo.org/records/11813 (2014)
- Poznanski, D., Prochaska, J. X. & Bloom, J. S. An empirical relation between sodium absorption and dust extinction. Mon. Not. R. Astron. Soc. 426, 1465–1474 (2012).
- Schlafly, E. F., & Finkbeiner, D. P. Measuring reddening with Sloan Digital Sky Survey stellar spectra and recalibrating SFD. Astrophys. J. 737, 103 (2011).
- 46. Burrows, D. N. et al. The Swift X-Ray Telescope. Space Sci. Rev. 120, 165–195 (2005).
- Azalee Bostroem, K. et al. Early spectroscopy and dense circumstellar medium interaction in SN 2023ixf. Astrophys. J. Lett. 956, L5 (2023).
- Dessart, L., Hillier, D. J., & Audit, E. Explosion of red-supergiant stars: influence of the atmospheric structure on shock breakout and early-time supernova radiation. Astron. Astrophys. 605, A83 (2017).
- Leonard, D. C., Filippenko, A. V., Barth, A. J. & Matheson, T. Evidence for asphericity in the Type IIN supernova SN 1998S. Astrophys. J. 536, 239 (2000).
- Fassia, A. et al. Optical and infrared spectroscopy of the type IIn SN 1998S: days 3–127.
   Mon. Not. R. Astron. Soc. 325, 907–930 (2001).
- Terreran, G. et al. The early phases of supernova 2020pni: shock ionization of the nitrogen-enriched circumstellar material. Astrophys. J. 926, 20 (2022).
- Jacobson-Galán, W. V. et al. Final moments. I. Precursor emission, envelope inflation, and enhanced mass loss preceding the luminous Type II supernova 2020tlf. Astrophys. J. 924, 15 (2022).
- Vasylyev, S. S. et al. Early time spectropolarimetry of the aspherical Type II supernova SN 2023ixf. Astrophys. J. Lett. 955, L37 (2023).
- Berger, E. et al. Millimeter observations of the Type II SN 2023ixf: constraints on the proximate circumstellar medium. Astrophys. J. Lett. 951, L31 (2023).
- Morag, J., Sapir, N. & Waxman, E. Shock cooling emission from explosions of red supergiants – I. A numerically calibrated analytic model. Mon. Not. R. Astron. Soc. 522, 2764–2776 (2023).
- Hosseinzadeh, G. et al. Shock cooling and possible precursor emission in the early light curve of the Type II SN 2023ixf. Astrophys. J. Lett. 953, L16 (2023).
- Hiramatsu, D. et al. From discovery to the first month of the Type II supernova 2023ixf: high and variable mass loss in the final year before explosion. Astrophys. J. 955, L8 (2023).

- Singh Teja, R. et al. Far-ultraviolet to near-infrared observations of SN 2023ixf: a highenergy explosion engulfed in complex circumstellar material. Astrophys. J. 954, L12 (2023).
- Soraisam, M. D. et al. The SN 2023ixf progenitor in M101. I. Infrared variability. Astrophys. J. 957, 64 (2023).
- Flinner, N., Tucker, M. A., Beacom, J. F. & Shappee, B. J. No UV-bright eruptions from SN 2023ixf in GALEX imaging 15–20 yr before explosion. Res. Notes AAS 7, 174 (2023).
- Fransson, C. UV and X-ray emission from Type II supernovae. Bull. Am. Astron. Soc. 14, 935 (1982).
- Fransson, C. et al. High-density circumstellar interaction in the luminous Type IIn SN 2010il: the first 1100 days. Astrophys. J. 797, 118 (2014).
- 2010jl: the first 1100 days. *Astrophys. J.* **797**, 118 (2014).
  63. Kurucz, R. L. An atomic and molecular data bank for stellar spectroscopy. *ASP Conf. Ser.*

81. 583 (1995).

 Yaron, O. & Gal-Yam, A. WISeREP—an interactive supernova data repository. Publ. Astron. Soc. Pac. 124, 668–681 (2012).

Acknowledgements We thank B. Katz and E. Waxman for their advice on the physical interpretation of SN2023ixf. This work is based on observations obtained with HST as part of proposal GO-17205 (PI E. Zimmerman). Based in part on observations obtained with the Samuel Oschin 48-inch telescope and the 60-inch telescope at the Palomar Observatory as part of the Zwicky Transient Facility (ZTF) project. The ZTF is supported by the U.S. National Science Foundation (NSF) under grant AST-2034437 and a collaboration including Caltech, IPAC, the Weizmann Institute of Science, the Oskar Klein Centre at Stockholm University, the University of Maryland, Deutsches Elektronen-Synchrotron and Humboldt University, the TANGO Consortium of Taiwan, the University of Wisconsin at Milwaukee, Trinity College Dublin, Lawrence Livermore National Laboratories, IN2P3, University of Warwick, Ruhr University Bochum and Northwestern University. Operations are conducted by COO. IPAC and UW. The SED Machine is based on work supported by the NSF under grant 1106171. Based in part on observations made with the Nordic Optical Telescope (NOT), owned in collaboration by the University of Turku and Aarhus University and operated jointly by Aarhus University, the University of Turku and the University of Oslo (representing Denmark, Finland and Norway, respectively), the University of Iceland and Stockholm University, at the Observatorio del Roque de los Muchachos, La Palma, Spain, of the Instituto de Astrofisica de Canarias. These data were obtained with ALFOSC, which is provided by the Instituto de Astrofisica de Andalucia (IAA) under a joint agreement with the University of Copenhagen and NOT. Some of the data presented herein were obtained at the W. M. Keck Observatory, which is operated as a scientific partnership among the California Institute of Technology, the University of California and the National Aeronautics and Space Administration (NASA); the Observatory was made possible by the generous financial support of the W. M. Keck Foundation. This work includes observations obtained at the Liverpool Telescope, which is operated on the island of La Palma by Liverpool John Moores University in the Spanish Observatorio del Roque de los Muchachos of the Instituto de Astrofisica de Canarias, with financial support from the UK Science and Technology Facilities Council. A major upgrade of the Kast spectrograph on the Shane 3-m telescope at Lick Observatory, led by B. Holden, was made possible through generous gifts from the Heising-Simons Foundation, William and Marina Kast and the University of California Observatories. Research at Lick Observatory is partially supported by a generous gift from Google. This work benefited from the OPTICON telescope access programme (https://www. astro-opticon.org/index.html), financed from the European Union's Horizon 2020 research and innovation programme under grant agreement 101004719. Based in part on observations made with the Italian Telescopio Nazionale Galileo (TNG) operated on the island of La Palma by the Fundación Galileo Galilei of the Istituto Nazionale di Astrofisica (INAF) at the Spanish Observatorio del Roque de los Muchachos of the Instituto de Astrofisica de Canarias. This research used data obtained with the Dark Energy Spectroscopic Instrument (DESI). DESI construction and operations is managed by the Lawrence Berkeley National Laboratory. This material is based upon work supported by the US Department of Energy, Office of Science, Office of High-Energy Physics, under contract no. DE-ACO2-05CH11231, and by the National Energy Research Scientific Computing Center, a DOE Office of Science User Facility under the same contract. Additional support for DESI was provided by the U.S. National Science Foundation (NSF), Division of Astronomical Sciences under contract no. AST-0950945 to the

NSF's National Optical-Infrared Astronomy Research Laboratory: the Science and Technology Facilities Council of the United Kingdom; the Gordon and Betty Moore Foundation; the Heising-Simons Foundation; the French Alternative Energies and Atomic Energy Commission (CEA); the National Council of Science and Technology of Mexico (CONACYT); the Ministry of Science and Innovation of Spain (MICINN), and by the DESI Member Institutions: www.desi.lbl. gov/collaborating-institutions. The DESI collaboration is honoured to be permitted to conduct scientific research on Iolkam Du'ag (Kitt Peak), a mountain with particular significance to the Tohono O'odham Nation. Any opinions, findings, and conclusions or recommendations expressed in this material are those of the author(s) and do not necessarily reflect the views of the US National Science Foundation, the US Department of Energy, or any of the listed funding agencies. We made use of IRAF, which is distributed by the NSF NOIR Lab. The Gordon and Betty Moore Foundation, through both the Data-Driven Investigator Program and a dedicated grant, provided critical funding for SkyPortal. A.V.F.'s supernova group at University of California, Berkeley has been supported by S. Nelson, G. and C. Bengier, C. and S. Winslow, S. Robertson, B. and K. Wood, the Christopher R. Redlich Fund and numerous other donors. T.S. acknowledges support from the Comunidad de Madrid (2022-T1/TIC-24117).

Author contributions E.A.Z. is the PI of the HST proposal, triggered the HST observations,  $reduced \ the \ HST \ spectra, \ conducted \ follow-up \ observations, \ conducted \ spectroscopic \ and$ physical analysis and wrote the manuscript, I.I. helped develop the manuscript, contributed to follow-up design and execution, conducted photometric analysis and physical analysis reduced the saturated Swift data and contributed to the physical interpretation of the data P.C. contributed to follow-up design and execution, reduced photometry and reduced the Swift spectra. A.G.-Y. leads the Weizmann research group, provided mentorship and edited the manuscript. S.Sc. conducted spectroscopic analysis and reduced the XRT data. D.A.P. classified the supernova and provided Liverpool Telescope data. J.S. helped develop the manuscript, provided the NOT data and is a ZTF builder. A.V.F. leads the University of California, Berkeley research group, is PI of the Lick programme and thoroughly edited the manuscript. T.S. modelled the SN spectra and advised on spectral analysis, O.Y. helped develop the manuscript and created several figures. S.Sh. provided microtelluric models for the HARPS spectra and advised on statistical tests. R.J.B. contributed to follow-up design and execution and helped develop the manuscript. E.O.O. advised on the physical interpretation and helped develop the manuscript. A.D.C. conducted an analysis of the interstellar-medium absorption lines. T.G.B. obtained and reduced all of the Lick data. Y.Y. and S.S.V. helped develop the manuscript, S.B.A. contributed to follow-up design and execution, M.A. is part of the ZTF calibration team, A.B. advised on the measurement of Na extinction, J.S.B. and K.Z. obtained data for this study, P.J.B. and M.R. consulted on Swift data reduction and helped develop the manuscript, M.M.K. and K.D. provided infrared data from Gattini and IRTE, G.D., J.H.T. and K.M.S. obtained the INT spectrum, C.Fra. advised on the physical interpretation, and helped develop the manuscript, C.Fre, requested and shared the KCWI data, A.H. and I.S. advised on radio data. K.H. and J.W. reduced Liverpool Telescope data. J.P.J. obtained the NOT/FIES spectra. S.R.K. is the 7TE Pland contributed Keck data, D.K., LM, and TW, advised on the physical interpretation and models. J.D.N. obtained and reduced the KCWI data. C.M., M.M., N.Z.P. and R.C.M. are part of the KCRM commissioning team and were involved in obtaining the KCWI data. P.E.N. provided the DESI data and contributed to follow-up design and execution. L.Y. and A.A.M. helped develop the manuscript and are co-authors of HST proposal GO-17205. R.S.P. provided photometry from the Post Observatory, Mayhill, NM. Y.Q. and R.D.S. provided and reduced Keck spectroscopic data. A.R. reduced the DESI spectra. R.R. and B.R. are ZTF builders. M.S. is a co-author of HST proposal GO-17205. A.W. is part of the ZTF data-system team. K.D. is a NASA Einstein Fellow.

Competing interests The authors declare no competing interests.

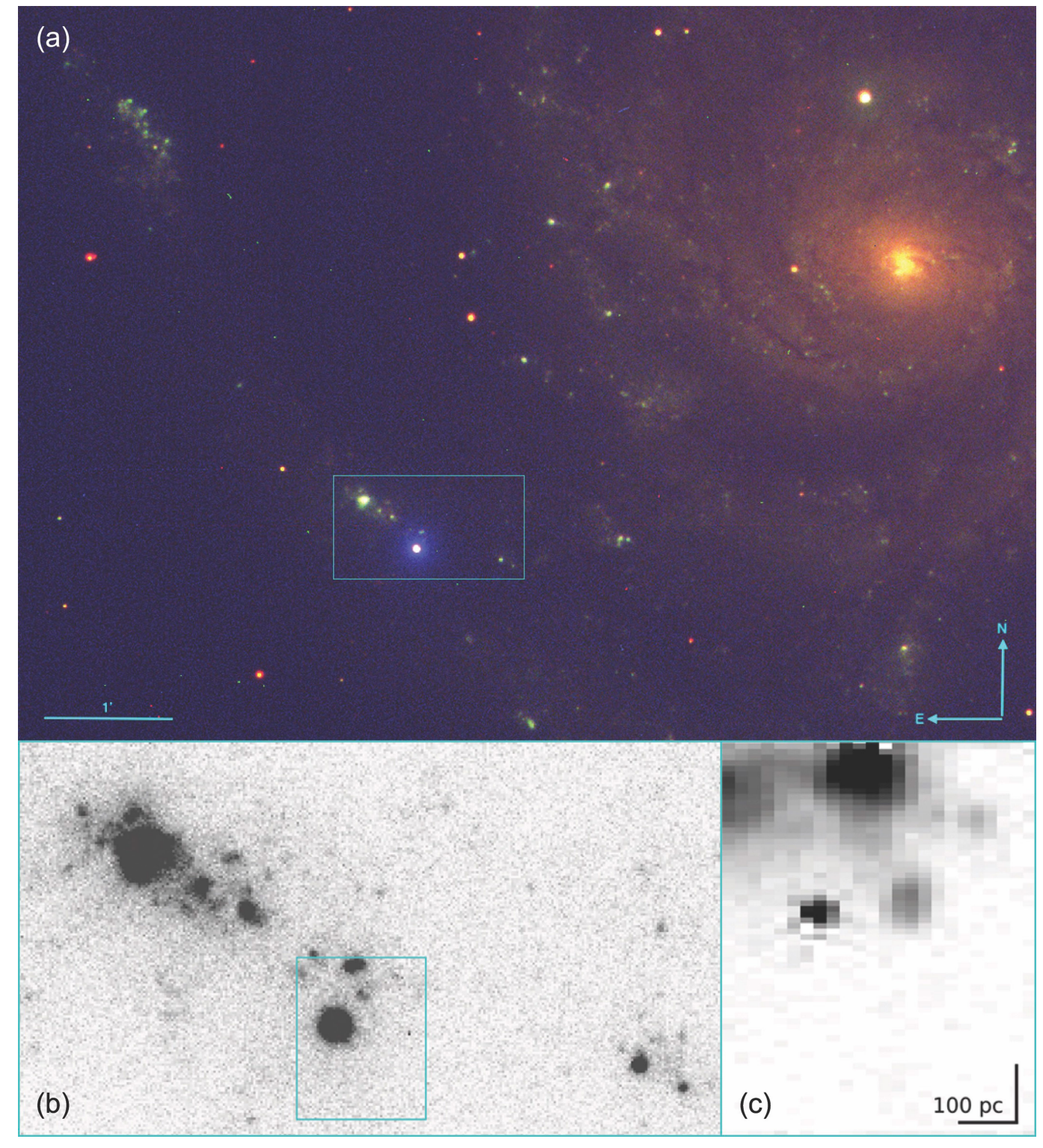
#### Additional information

 $\textbf{Supplementary information} \ The online version contains supplementary material available at https://doi.org/10.1038/s41586-024-07116-6.$ 

Correspondence and requests for materials should be addressed to E. A. Zimmerman.

Peer review information Nature thanks the anonymous reviewers for their contribution to the peer review of this work. Peer reviewer reports are available.

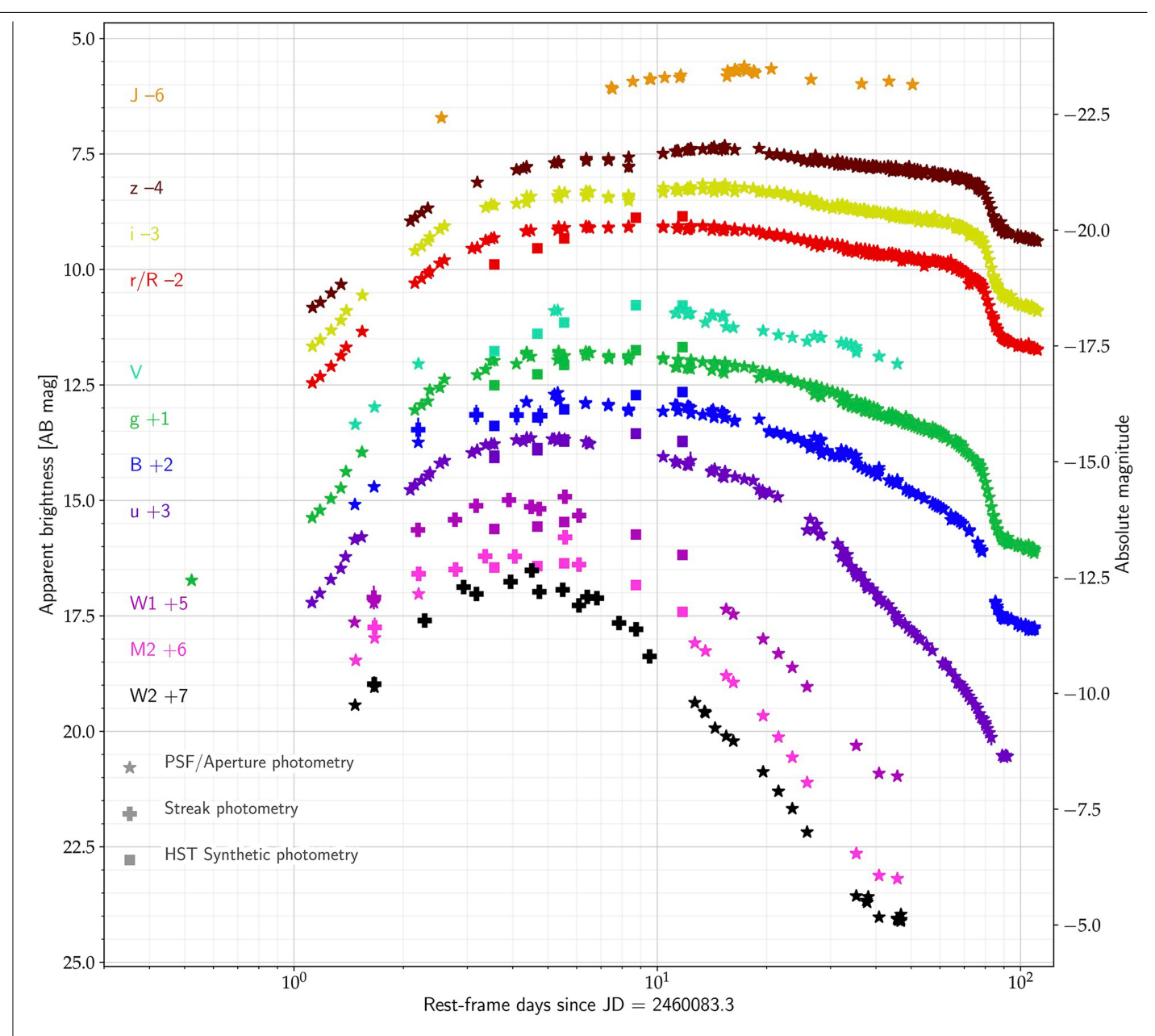
Reprints and permissions information is available at http://www.nature.com/reprints.



 $Extended\ Data\ Fig.\ 1 | Location\ of\ SN\ 2023 ix fwithin\ the\ M101 galaxy.$ 

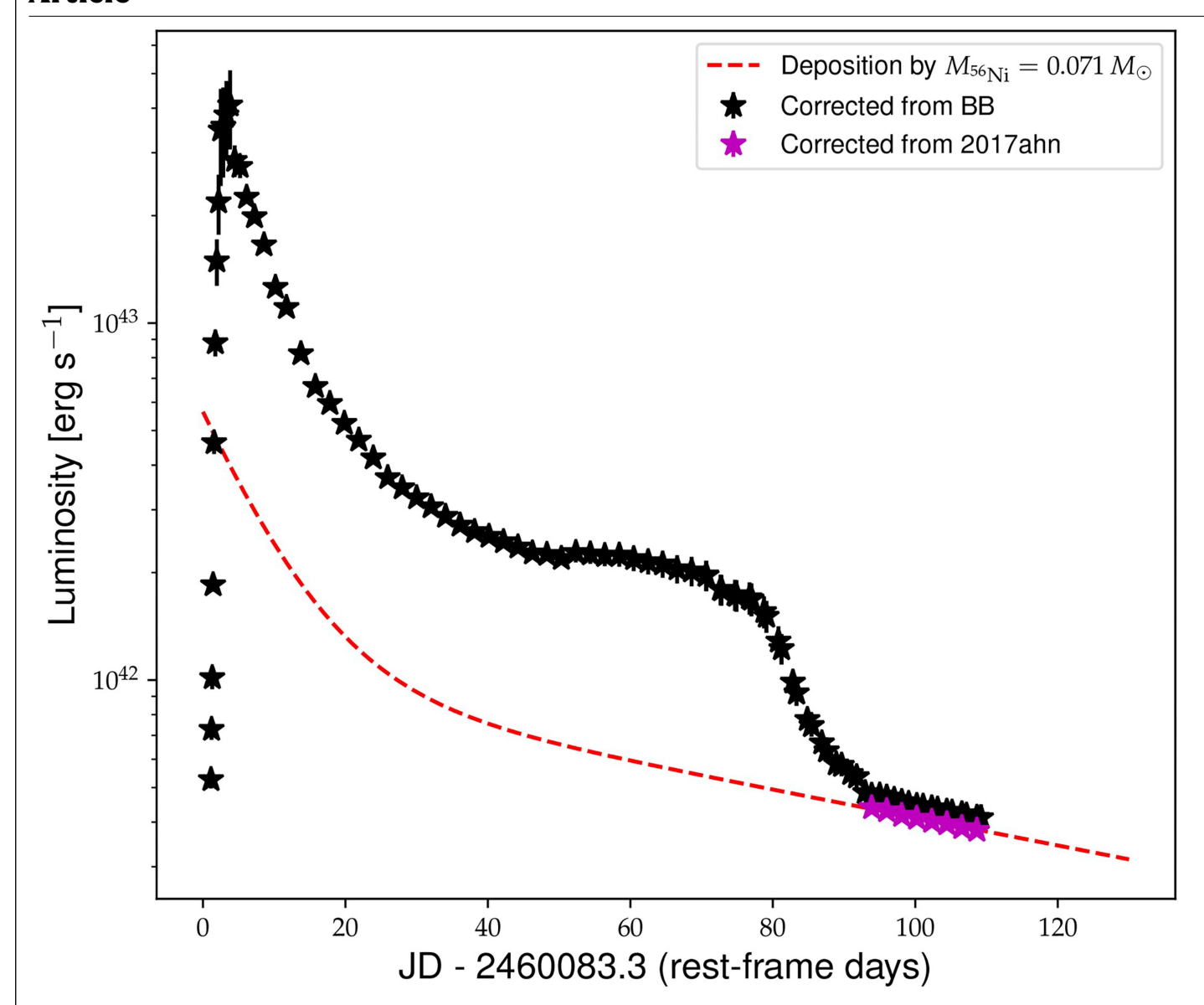
 $\label{eq:approx} \textbf{a}, A composite ugi image taken by the Liverpool Telescope showing the location of SN 2023ixf within the M101 galaxy. The SN is clearly seen to be very blue (the most blue object within the inset rectangle). It is located within a spiral arm at the outskirts of the galaxy. <math display="block">\textbf{b}, \text{The Liverpool Telescope} \ g\text{-band image showing}$  the area marked in the composite image. Nearby star-forming regions are

clearly seen. c,  $H\alpha$  image of the direct vicinity of SN 2023ixf, as marked in the Liverpool Telescope g-band image, constructed from observations with the integral field unit KCWI. The SN explosion site is embedded in a region of continuing star formation, including diffusely distributed lower-level star-formation activity and islands of enhanced star formation.



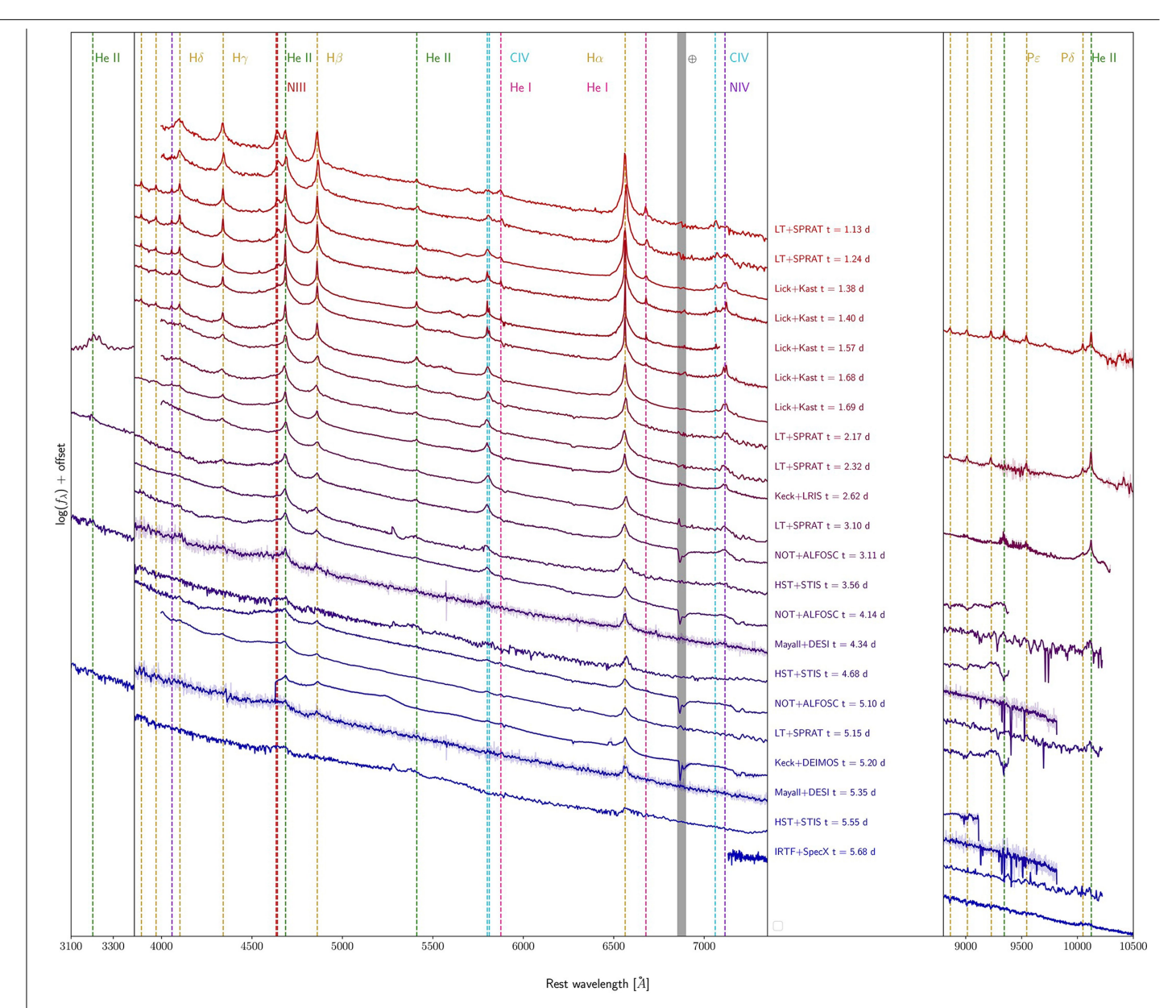
 $\textbf{Extended Data Fig. 2} | \textbf{UV-optical light curves of SN 2023ixf.} \ Point spread function or aperture photometry is shown with star symbols, UVOT streak photometry is indicated using a plus symbol and synthetic photometry from$ 

HST is indicated using squares. The marker colours correspond to the band filter indicated on the left side of the figure. The error bars are of  $1\sigma$  standard deviation.



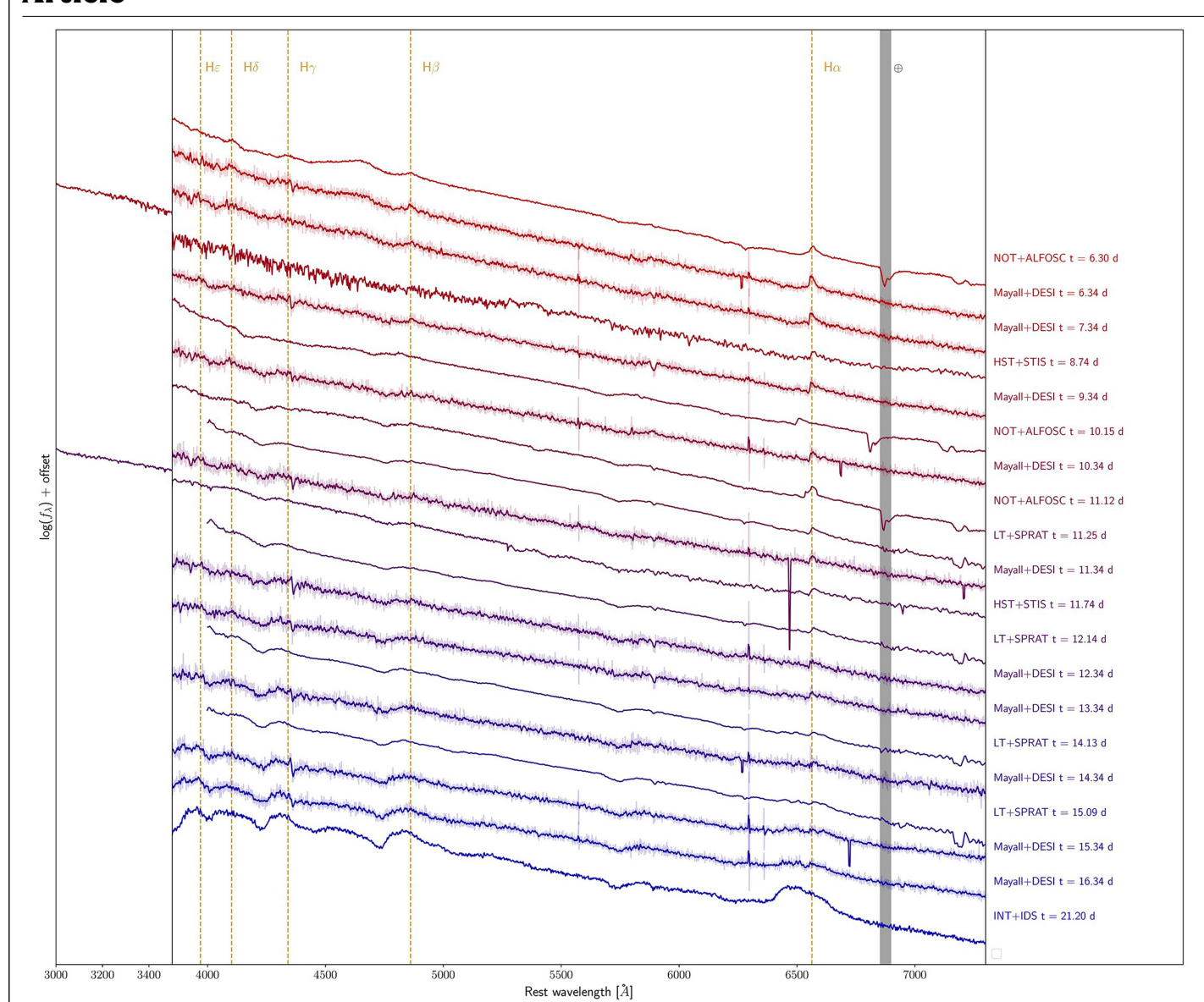
 $\label{lem:extended} \textbf{Data} \textbf{Fig. 3} | \textbf{Bolometric light curve of SN 2023ixf.} \text{ The black stars } \\ represent the reconstructed bolometric light curves using a blackbody \\ extrapolation. The error bars are of $1\sigma$ standard deviation. The magenta points \\ are the late-time bolometric luminosity reconstructed using the bolometric \\ \end{tabular}$ 

correction of SN 2017ahn to the uBgriz late-time pseudo bolometric light curve. The dashed red line indicates the energy deposition from the best-fit  $^{56}$ Ni mass (labelled in the legend; see Methods section 'Photometry') to the  $t\!>\!90\text{-}\text{day}$  luminosity. Error bars are  $1\sigma$  standard deviations.

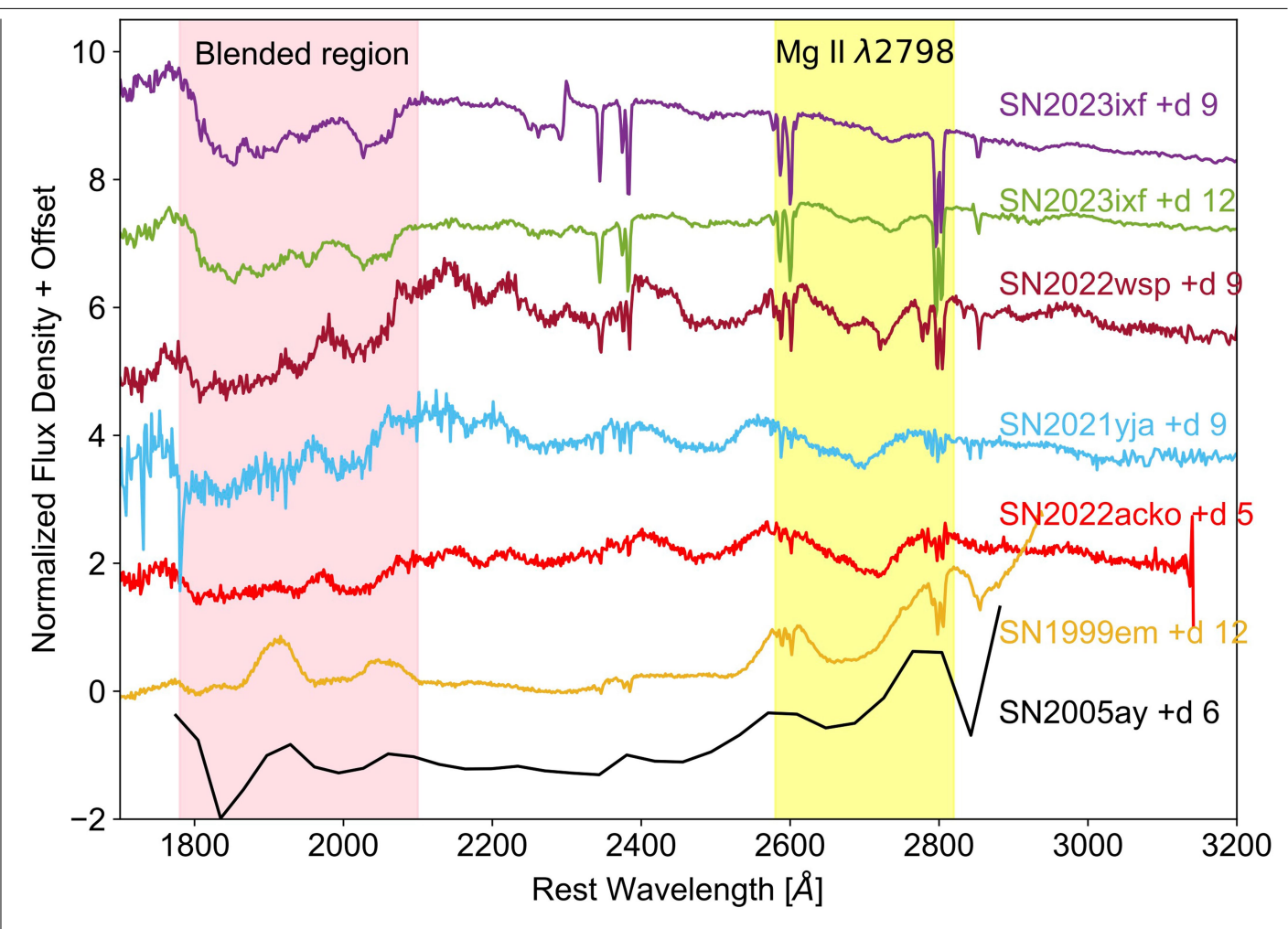


**Extended Data Fig. 4** | **The early-time spectral sequence of SN 2023ixf.**A plethora of narrow flash-ionization lines is seen in the earliest spectra, including the H Balmer series, H Paschen series, several series of He II

 $(n\to3,4,5,6),$  He I, C IV, N IV, N III and C III. Lower-ionization species (C III, N III, He I) weaken until they disappear in the optical spectra by day 2.

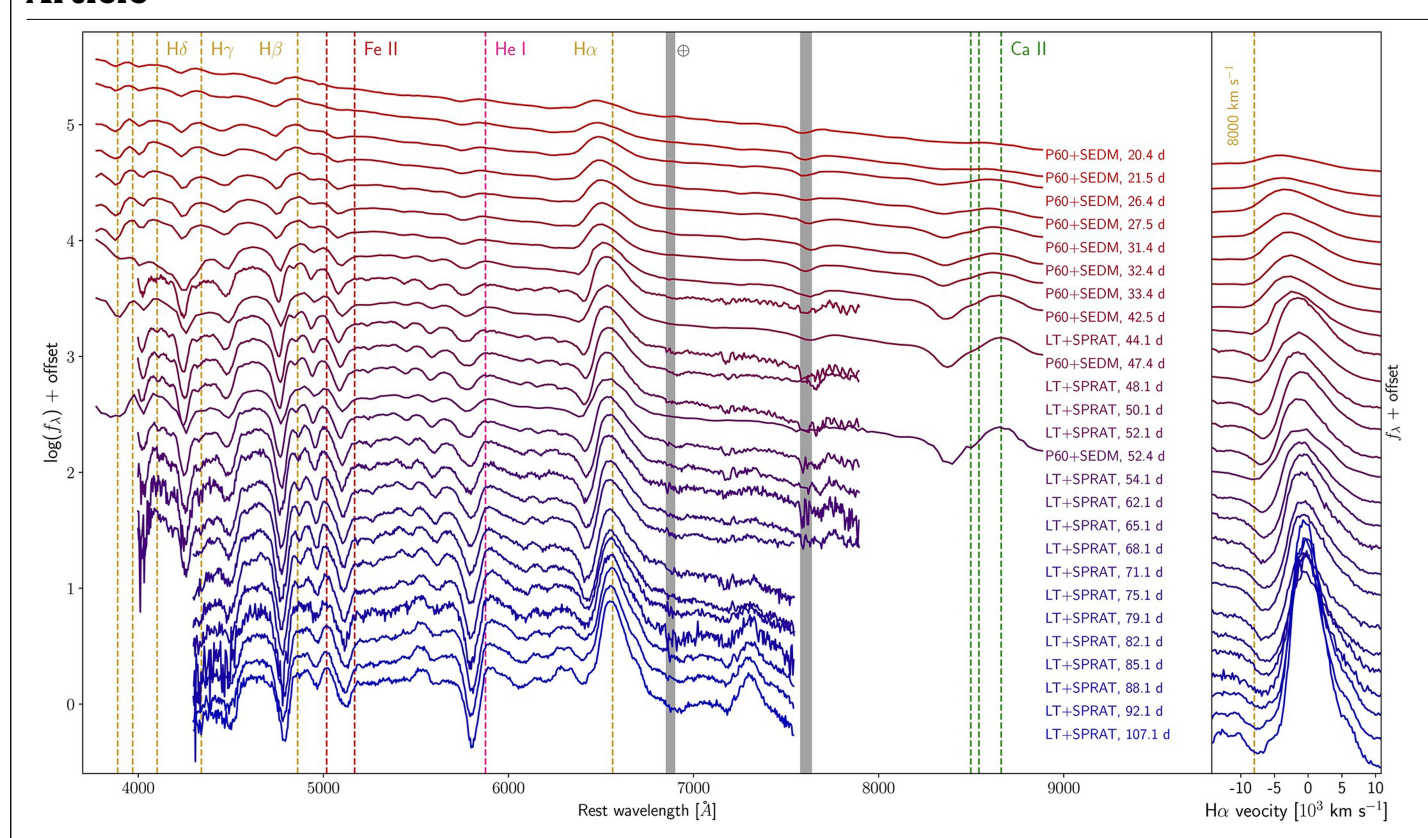


**Extended Data Fig. 5** | **The early spectral sequence of SN 2023 ix fafter** t = 6 **days and until broad features appear.** All narrow lines except narrow H $\alpha$  P Cygni disappear by day 6 in the optical. The narrow P Cygni no longer appears by approximately day 16.

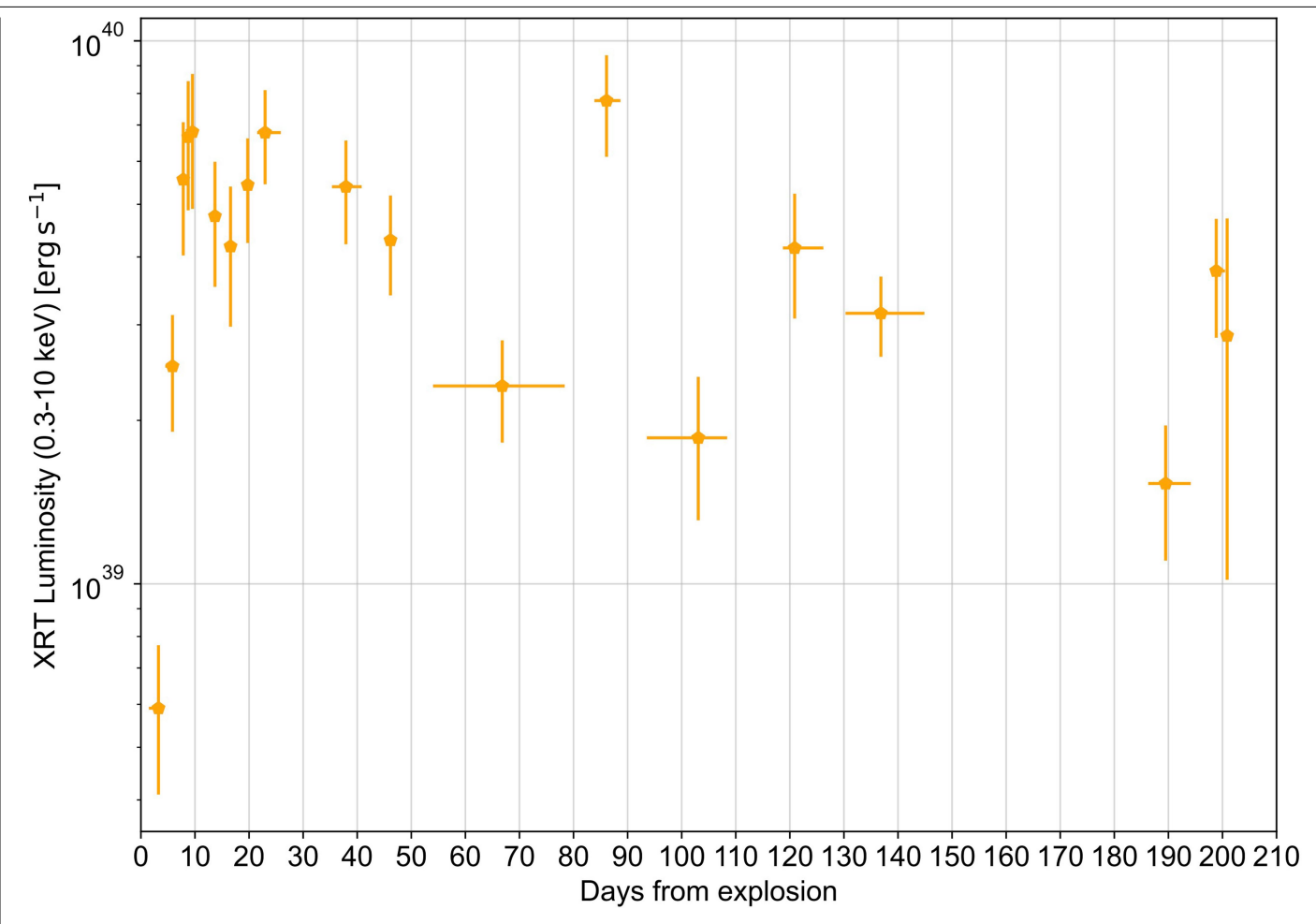


**Extended Data Fig. 6** | **Early photospheric UV spectra of SN 2023ixf and other Type II SNe.** The early-time UV spectra of SN 2022wsp (ref. 37), SN 2021yja (ref. 38), SN 2022acko (ref. 39), SN 1999em (ref. 40) and SN 2005ay (ref. 41) are presented. All spectra were taken by HST except for the SN 2005ay spectrum obtained with GALEX. The prominent Mg II $\lambda$ 2798 line is marked in yellow. Its double-peaked shape is similar to that of SN 2022wsp, indicating an Fe II transition<sup>37</sup>. The broad absorption across 1,800–2,100 Å is marked as well

and arises from a mix of metals. The features in SN 2023ixf are similar to those of SN 2022wsp, SN 2021yja and SN 2022acko, yet shifted because of different velocity regimes. The uniformity of these features suggests that they originate from the natal chemical composition of the exploding star. However, a strong emission feature at roughly 1,910  $\rm \mathring{A}$  appears in the spectra of SN 1999em and SN 2005ay, suggesting that some diversity in SN II UV photospheric features exists as well.

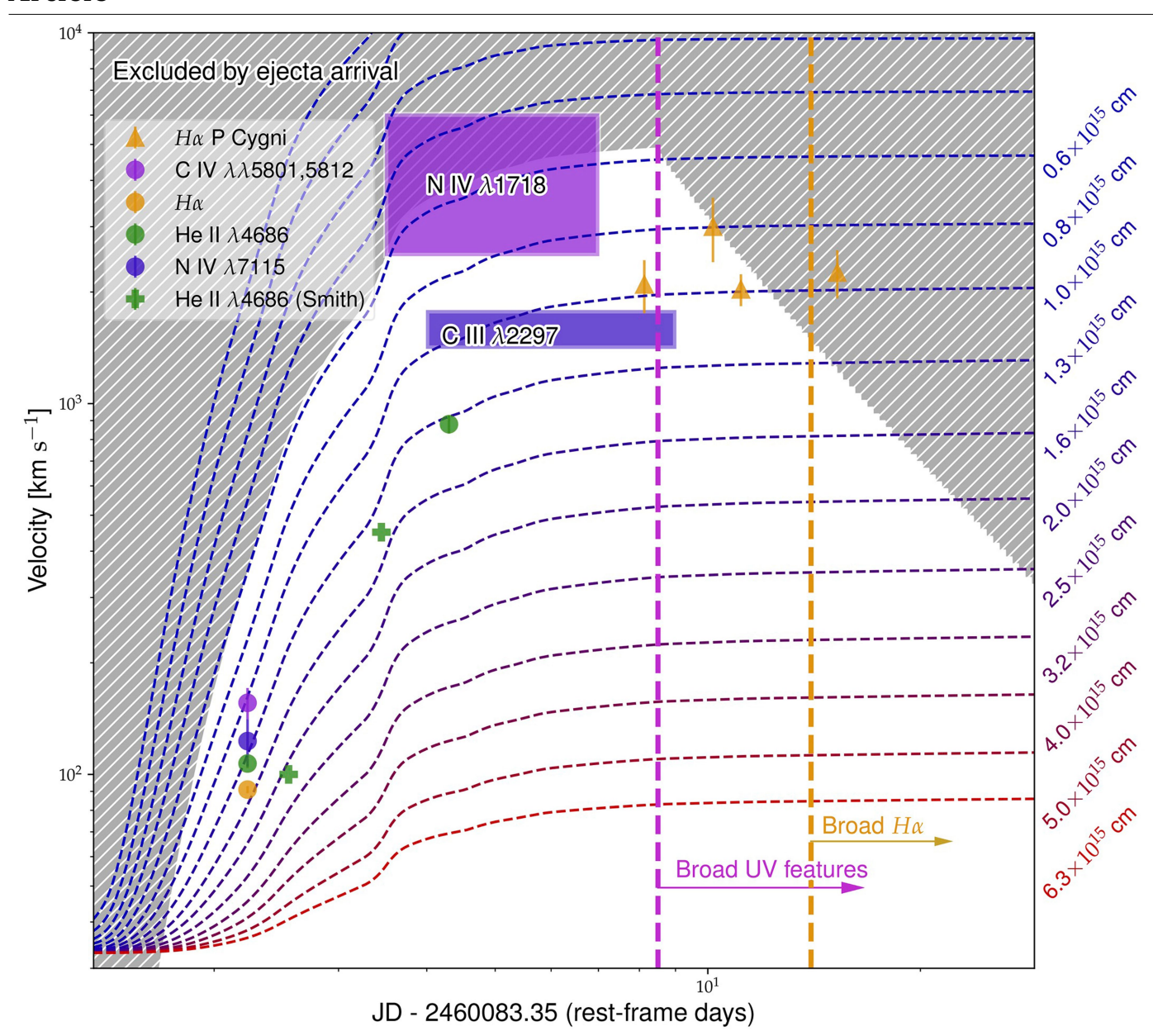


**Extended Data Fig. 7**| **Photospheric-phase spectra of SN 2023ixf.** The photospheric development of the SN is typical of Type II-P SNe. A zoom-in of the H $\alpha$ P Cygni profile is presented in the right panel, with 8,000 km s<sup>-1</sup> H $\alpha$  marked. We adopt this value as the early-time ejecta velocity.



**Extended Data Fig. 8** | **X-ray light curve of SN 2023ixffrom XRT.** The absorbed X-ray luminosity from the XRT 0.3-10-keV band is presented. Each point represents a binned measurement, with an error bar representing the

measurement period. The relatively constant X-ray luminosity suggests an average CSM density profile  $\rho \propto r^2$ . The error bars show a  $1\sigma$  standard deviation.



**Extended Data Fig. 9** | **Narrow-line-velocity evolution of SN 2023ixf.** Feature velocities and appearance times for H $\alpha$ , He II $\lambda$ 4686, N IV  $\lambda$ 1718 and C III $\lambda$ 2297 are presented. The dashed lines show the expected radiative acceleration of stationary matter at  $\tau$  < 1, calculated from the cumulative

radiated energy at different radii. We indicate the region excluded by ejecta starting at  $R_{\rm bo}/2 = 0.8 \times 10^{14}$  cm with a velocity of  $10^9$  cm s<sup>-1</sup>, estimated from the blue edge of the photospheric spectrum. Previous approximate measurements<sup>19</sup> are added as well. The error bars show a  $1\sigma$  standard deviation.